

Water Resources Research®

RESEARCH ARTICLE

10.1029/2021WR030031

Key Points:

- An integrated framework is proposed to estimate global irrigation water use (IWU) from multiple satellite-based products
- The IWU estimation scheme can capture the trends of irrigation dynamics well during the study period
- The underestimation in global IWU can be mainly attributed to the coarse resolution of the satellite-based products

Supporting Information:

Supporting Information may be found in the online version of this article.

Correspondence to:

X. Li and D. Zheng,
xinli@itpcas.ac.cn;
zhengd@itpcas.ac.cn

Citation:

Zhang, K., Li, X., Zheng, D., Zhang, L., & Zhu, G. (2022). Estimation of global irrigation water use by the integration of multiple satellite observations. *Water Resources Research*, 58, e2021WR030031. <https://doi.org/10.1029/2021WR030031>

Received 25 MAR 2021

Accepted 7 MAR 2022

Author Contributions:

Conceptualization: Kun Zhang, Xin Li
Formal analysis: Kun Zhang, Donghai Zheng, Ling Zhang
Investigation: Xin Li, Ling Zhang, Gaofeng Zhu
Methodology: Kun Zhang, Donghai Zheng, Ling Zhang, Gaofeng Zhu
Project Administration: Kun Zhang, Xin Li
Resources: Xin Li
Supervision: Xin Li
Validation: Kun Zhang
Visualization: Kun Zhang
Writing – original draft: Kun Zhang
Writing – review & editing: Xin Li, Donghai Zheng, Ling Zhang, Gaofeng Zhu

© 2022. American Geophysical Union.
All Rights Reserved.

Estimation of Global Irrigation Water Use by the Integration of Multiple Satellite Observations

Kun Zhang^{1,2,3} , Xin Li¹ , Donghai Zheng¹ , Ling Zhang⁴ , and Gaofeng Zhu⁵ 

¹National Tibetan Plateau Data Center (TPDC), State Key Laboratory of Tibetan Plateau Earth System, Environment and Resources (TPESER), Institute of Tibetan Plateau Research, Chinese Academy of Sciences, Beijing, China, ²Department of Mathematics, The University of Hong Kong, Hong Kong, China, ³School of Biological Sciences, The University of Hong Kong, Hong Kong, China, ⁴Key Laboratory of Remote Sensing of Gansu Province, Northwest Institute of Eco-Environment and Resources, Chinese Academy of Sciences, Lanzhou, China, ⁵College of Earth and Environmental Sciences, Lanzhou University, Lanzhou, China

Abstract Quantification of the global irrigation water use (IWU) is crucial to understanding the anthropogenic disturbance of the natural hydrological cycle and optimal agricultural water management. However, it is challenging to obtain time series data with the conventional survey-based approach, while the current satellite-based IWU estimations are subject to data gaps and the model structure. In this paper, we propose a comprehensive framework to couple the different processes associated with irrigation and integrate multiple satellite observations to estimate the global IWU. The ensemble IWU estimate demonstrates an improved performance when compared to the IWU obtained from individual satellite observations. The results show reasonable correlation with the survey-based irrigation water withdrawal in states of the US (bias = -0.42 km^3), provinces of China (bias = -3.10 km^3), and country statistics from the Food and Agriculture Organization (bias = -10.84 km^3). Large amounts of IWU are apparent in India, China, the US, Europe, and Pakistan, making up $>70\%$ of the global IWU. A general underestimation of IWU is found both in this work and previous studies, due to the coarse resolution and asynchronism of the various satellite products, the changes in irrigated areas, and the deficiency in detecting irrigation events under the case of saturated soil moisture. Nevertheless, we demonstrate advantages in integrating multiple satellite observations to reduce the uncertainty in estimating global IWU. However, additional efforts are needed to produce high-quality and finer spatiotemporal resolution satellite-based products, to further improve the accuracy of the global IWU estimation.

1. Introduction

As the largest freshwater consumer, agricultural irrigation consumes about 70% of the global freshwater withdrawal from surface/subsurface water systems, representing the most significant human-driven alteration to the natural hydrological cycle (Foley et al., 2011; Siebert et al., 2010). Meanwhile, to sustain an ever-increasing global population, agriculture's expansion requires more and more water for irrigation (Jägermeyr et al., 2017). Moreover, the localized water and energy balance can be affected by irrigation when it artificially increases evapotranspiration (ET), leading to a decrease in the sensible heat flux and cooling of the air temperature, which can partly attenuate the warming effect induced by greenhouse gases (Bonfils & Lobell, 2007; Lawston et al., 2017; Zaussinger et al., 2019). Therefore, accurate estimation of irrigation water use (IWU) and its spatiotemporal patterns is crucial for understanding regional water budgets and improving the efficiency of agricultural water management (Brocca et al., 2018; Jalilvand et al., 2019; Kumar et al., 2015; Li et al., 2018; Siebert et al., 2015; Wada et al., 2013, 2014, 2017). Knowledge of IWU is also beneficial when exploring the hydrologic implications of human activities, such as ET redistribution (Fisher et al., 2017), local cooling effects (Kueppers et al., 2007), and irrigation efficiency at multiple scales (Grafton et al., 2018).

In the past few decades, remote sensing techniques have evolved rapidly, and have made the monitoring of irrigation by onboard sensors possible (AghaKouchak et al., 2015; Fisher et al., 2017). Nevertheless, quantification of the actual IWU has rarely been explored at a large scale, which represents the total irrigation water actually entering the field (including the irrigation water consumption (IWC) supporting plant growth, soil evaporation, canopy interception of water, and soil water drainage). A novel way of estimating IWU has been recently proposed through identifying the soil moisture changes caused by rainfall and irrigation events (Brocca et al., 2018). By

treating the irrigation event as a special type of rainfall, Brocca et al. (2013) proposed the SM2RAIN algorithm to estimate the total water that falls on the irrigated land. This algorithm has since been widely evaluated at multiple scales (Brocca et al., 2016; Ciabatta et al., 2017; Prakash, 2019; Zhang et al., 2020). Thus, the amount of IWU can be determined when the soil moisture increases on rain-free days.

However, there are still some limitations to this method, especially when estimating IWU at a global scale. First, to apply this method to estimate global IWU, the primary issue is the inevitable data gaps in the individual satellite-based soil moisture product induced by the satellite orbit and data quality. However, there are now various microwave remote sensing products suitable for use in global applications, which provide us with the potential for incorporating the advantages of the various soil moisture products, to reduce the data gaps/errors arising from individual observations (Dorigo et al., 2010; Liu et al., 2012). Hence, it is imperative to integrate the various available satellite-based soil moisture products when estimating IWU at a global scale. Second, the ET process in the previous studies has been simply characterized as either an empirical relationship with air temperature or a linear constraint to potential ET by soil moisture (Brocca et al., 2018; Jalilvand et al., 2019), which can cause uncertainty when estimating the soil water balance, and thus IWU. Therefore, it is necessary to incorporate a process-based ET model, such as the Priestley-Taylor Jet Propulsion Laboratory (PT-JPL) model (Fisher et al., 2008), to quantify the spatiotemporal distribution of global ET. Finally, the accurate estimation of global IWU is also greatly dependent on the proper selection of model parameters when connecting the different variables associated with the soil water balance. Recently, Bayesian methods have received much attention in the parameter estimation of nonlinear models (Clark & Gelfand, 2006; Keating et al., 2010; Zhang et al., 2019; Zhu et al., 2014). By combining the prior knowledge of the parameters and observations, the posterior distribution of the parameters can be obtained by the Bayesian methods (Zhu et al., 2018). However, to date, no related studies have been conducted with regard to optimizing the parameters in IWU estimation by the use of the Bayesian methods.

Therefore, in this study, we attempted to estimate the amount of IWU in global irrigated areas by integrating various satellite-based soil moisture and precipitation products. The main objectives of this study were to: (a) develop a physically based framework for the estimation of global IWU with multiple satellite observations; (b) improve the performance of IWU estimation by coupling a process-based ET module and utilizing a Bayesian data/model fusion scheme; and (c) establish the spatial and temporal patterns of global IWU. In addition, in this paper, the estimated IWU is further compared with the available irrigation inventories, and the uncertainties associated with the estimation are also identified.

2. Methods

2.1. Theoretical Foundation for the Estimation of IWU

For a daily interval, the changes in soil water storage for a unit area can be expressed as (Dari et al., 2020; Filippucci et al., 2020; Jalilvand et al., 2019)

$$Z_s \frac{d\theta}{dt} = P(t) + I(t) - ET(t) - D(t) - S(t), \quad (1)$$

$$D(t) = K_s \cdot \theta(t)^{3+\frac{2}{b}}, \quad (2)$$

where θ is the relative soil moisture (%); Z_s is a parameter related to the soil physical characteristics (i.e., soil porosity and layer depth), which represents the maximum water storage capacity of the soil column; t is the time step (i.e., days); P is the precipitation (mm); I represents the amount of IWU (mm); ET is the evapotranspiration (mm), which includes the soil surface evaporation, plant transpiration, and evaporation through canopy interception; D is the drainage (mm), which includes both deep percolation and lateral infiltration; S is the surface runoff (mm), which can be ignored in irrigated cropland; K_s is the saturated hydraulic conductivity (mm); and b is the pore size distribution parameter.

Thus, the IWU can be estimated if the state variables (i.e., P , ET , θ) and involved parameters (e.g., Z_s , K_s , b) are known. In this study, both P and θ were obtained from the satellite-based products, while the parameters (e.g., Z_s , K_s , b) in the models were optimized using the differential evolution Markov chain (DE-MC) scheme (see

Table 1
The Eco-Physiological Constraint Functions in the PT-JPL Model

Name	Description	Equation	Reference
f_{wet}	Relative surface wetness	RH^4	Fisher et al. (2008)
f_g	Green canopy fraction	$f_{\text{APAR}}/f_{\text{IPAR}}$	
f_m	Plant moisture constraint	$f_{\text{APAR}}/f_{\text{APARmax}}$	
f_{sm}	Soil moisture constraint	$\text{RH}^{\text{VPD}/\beta}$	
f_t	Plant growing temperature constraint	$\exp\left(-\left(\frac{T_a - T_{\text{opt}}}{T_{\text{opt}}}\right)^2\right)$	June et al. (2004)

Note. RH is the relative humidity (%); T_a is the air temperature ($^{\circ}\text{C}$); T_{opt} is the optimum temperature for plant growth ($^{\circ}\text{C}$); VPD is the vapor-pressure deficit (kPa); β is the sensitivity of f_{sm} to VPD; f_{IPAR} is the fraction of photosynthetically active radiation (PAR) intercepted by the canopy, which is derived from the normalized difference vegetation index (NDVI); f_{APAR} is the PAR absorbed by the green canopy, which is derived from the enhanced vegetation index (EVI).

Section 2.2). In this equation, ET is the key factor in determining the soil water conditions, and should be properly described. In this study, we used the process-based PT-JPL model to estimate ET.

The PT-JPL model based on the Priestly-Taylor (PT) equation (Priestley & Taylor, 1972) was initially developed by Fisher et al. (2008). In this model, the actual total ET is separated into plant transpiration (E_t), bare soil evaporation (E_s), and canopy-intercepted evaporation (E_i)

$$ET = E_t + E_s + E_i, \quad (3)$$

$$E_t = (1 - f_{\text{wet}}) \cdot f_g \cdot f_t \cdot f_m \cdot \alpha \frac{\Delta}{\lambda(\Delta + \gamma)} R_{\text{nc}}, \quad (4)$$

$$E_s = (f_{\text{wet}} + f_{\text{sm}}(1 - f_{\text{wet}})) \cdot \alpha \frac{\Delta}{\lambda(\Delta + \gamma)} (R_{\text{ns}} - G), \quad (5)$$

$$E_i = f_{\text{wet}} \cdot \alpha \frac{\Delta}{\lambda(\Delta + \gamma)} R_{\text{nc}}, \quad (6)$$

where α is the PT coefficient, which is equal to 1.26; Δ is the slope of the saturated vapor-pressure curve ($\text{kPa } ^{\circ}\text{C}^{-1}$); γ is the psychrometric constant ($0.066 \text{ kPa } ^{\circ}\text{C}^{-1}$); λ is the latent heat of vaporization (MJ kg^{-1}); G is the soil heat flux (W m^{-2}); R_{nc} and R_{ns} are the net radiation (R_n) allocated to plant canopy and soil surface, respectively; the f -function (i.e., $f_{\text{wet}}, f_g, f_t, f_m, f_{\text{sm}}$) represents the eco-physiological constraints (see Table 1). In this study, the input data of the PT-JPL model were obtained from reanalysis data sets and satellite-based products (see Section 3). The parameters of the PT-JPL model for cropland were directly derived from our previous work (Zhang et al., 2017).

2.2. Implementation of the IWU Algorithm

The main purpose of this study was to estimate the IWU on the pixels of the irrigated areas. In the IWU algorithm, there are three main steps when calculating IWU based on the estimates of the state variables and parameters in the soil water balance equation (Figure 1).

1. **Optimizing the parameters to balance the soil water dynamics:** First, we used satellite-based precipitation observations to estimate the parameters (i.e., $\phi = [Z_s, K_s, b]$) in Equation 1. On rainy days, we assumed that no irrigation was applied (i.e., $I = 0$). Thus, the precipitation can be derived based on the soil water balance equation as

$$P_{\text{der}}(\phi; t) = Z_s \frac{d\theta}{dt} + ET(t) + D(t), \quad (7)$$

where P_{der} is the derived precipitation from the soil water dynamics and ϕ is the vector of the unknown parameters. In this study, the changes in soil moisture ($\frac{d\theta}{dt}$) were acquired from the satellite observations, and ET

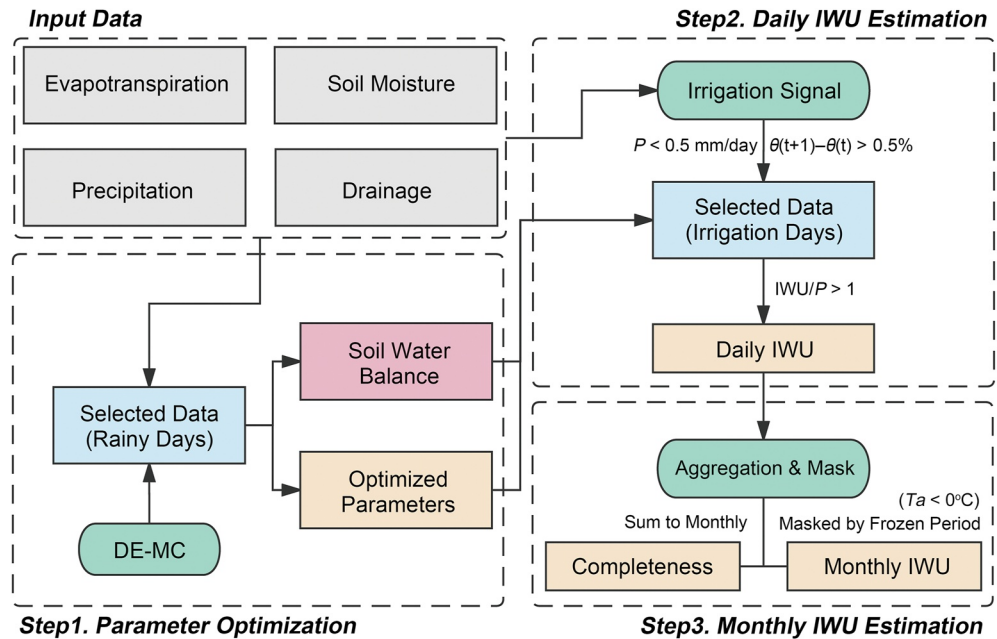


Figure 1. Diagram of the irrigation water use (IWU) estimation algorithm for each pixel of irrigated areas.

was obtained from the PT-JPL model. To optimize the unknown parameters (ϕ), we forced the values of P_{der} to be close to the target satellite-based precipitation observations (P_{obs}). In the Bayesian framework, the posterior distribution of the parameters can be expressed as

$$f(\phi|P_{\text{obs}}) = f(\phi) \prod_{t=1}^T \frac{1}{\sqrt{2\pi\sigma^2}} \exp\left(-\frac{(P_{\text{der}}(\phi; t) - P_{\text{obs}}(t))^2}{2\sigma^2}\right), \quad (8)$$

where $f(\phi|P_{\text{obs}})$ is the posterior parameter distributions; $f(\phi)$ is the prior parameter distributions; and σ is the standard deviation of the model error during the observation period. In this study, we employed the DE-MC scheme, which is a robust parameter optimization scheme, to obtain the optimal parameter values (the median values of the posterior distributions). The DE-MC scheme is an adaptive Markov chain Monte Carlo (MCMC) method, which is combined with a genetic algorithm (Storn & Price, 1997). In the DE-MC scheme, multiple chains are run in parallel to estimate the posterior distribution. For the i th iteration, the proposed chain is derived from two randomly selected chains, and the difference between them is multiplied by a scaling factor, which is then added to the current chain as

$$\phi_p = \phi_i + x(\phi_{r1} + \phi_{r2}) + e, \quad (9)$$

where ϕ_p is the proposed chain; ϕ_{r1} and ϕ_{r2} are two randomly selected chains without replacement from the population except ϕ_i ; x is the scaling factor, which is set as $\frac{2.38}{\sqrt{2d}}$ and d is the dimension of parameter sets; and e is drawn from a symmetrical distribution and represents a probabilistic acceptance rule. Additional details of the DE-MC scheme can be found in ter Braak and Vrugt (2008). In this study, we ran 20 chains in parallel and set a total of 5,000 iterations for each pixel, including 500 iterations as the burn-in period.

2. **Estimating the IWU at each pixel:** After obtaining the optimal parameter values, it is possible to estimate the IWU at each pixel based on the soil water balance relationship by identifying the irrigation signal. This approach has also been demonstrated in previous studies (Dari et al., 2020; Filippucci et al., 2020; Jalilvand et al., 2019). In particular, the increase in soil moisture is considered to be caused by irrigation when the precipitation is below a critical value (i.e., 0.5 mm day^{-1} ; Brocca et al., 2019). Thus, the daily IWU for a given pixel can be derived according to (Step 2 in Figure 1)

$$I(t) = Z_s \frac{d\theta}{dt} + ET(t) + D(t), \quad (10)$$

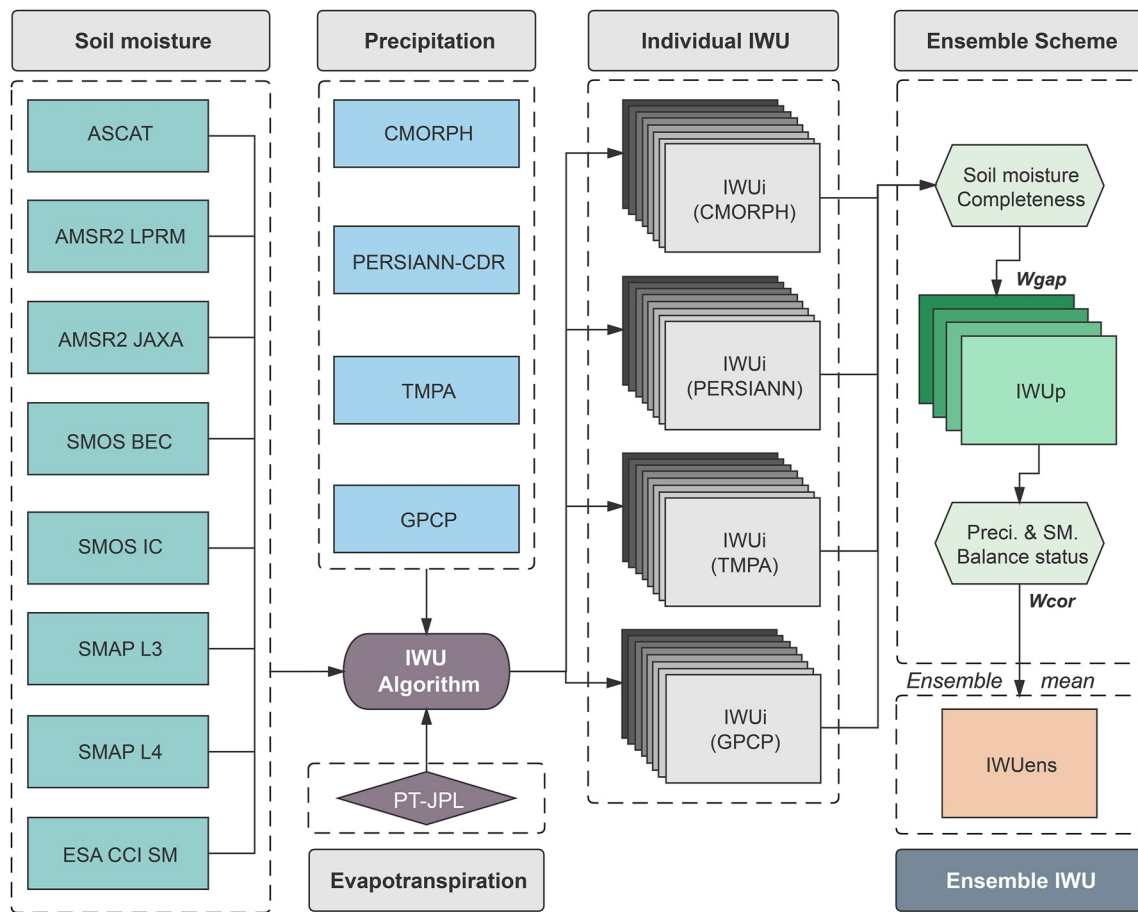


Figure 2. Framework for estimating global irrigation water use (IWU) based on multiple satellite-based products.

where $\frac{d\theta}{dt}$ is obtained from the satellite-based observations; ET is estimated using the PT-JPL model; and $D(t)$ can be estimated using the optimized parameters obtained in Step 1.

3. **Postprocessing:** We masked the daily IWU estimates during the frozen periods because no irrigation is applied when the air temperature is below 0°C (Step 3 in Figure 1). The daily IWU estimates were then aggregated to the monthly scale.

2.3. Framework for Integrating Multiple Satellite-Based Products

To overcome the data gaps and reduce the uncertainty caused by the input data, we used multiple satellite-based products to obtain ensemble estimates of IWU with a continuous coverage. Specifically, based on the IWU algorithm (Figure 1), a total of 32 groups of individual IWU (IWU_i) estimates were produced using the different satellite-based soil moisture products (eight) and precipitation products (four; Figure 2). However, these individual IWU estimates may be unreliable due to the data gaps caused by the satellite orbit coverage and noise (see Figure S1 in Supporting Information S1). To address this issue, we fused the different IWU_i estimates to obtain an ensemble IWU estimate. For a specific precipitation product, the individual monthly IWU was fused based on the corresponding completeness of the eight soil moisture products

$$IWU_p = \frac{1}{N} \sum_{i=1}^N (w_{gap}^i \cdot IWU_i), \quad (11)$$

where N is the number of soil moisture products ($N = 8$); IWU_i is the i th individual monthly IWU estimate ($i = 1, 2, \dots, 32$); IWU_p is the integrated estimate of IWU_i for the p th precipitation product (IWU_p) ($p = 1, 2, \dots, 4$); and

w_{gap}^i is the weight of IWU_i , which is derived from the completeness (c_i) of the different soil moisture products during the unfrozen period

$$w_{\text{gap}}^i = c_i / \sum_{i=1}^N c_i. \quad (12)$$

To further reduce the uncertainty of the precipitation products, a final ensemble IWU (IWU_{ens}) for each pixel was then determined as

$$\text{IWU}_{\text{ens}} = \frac{1}{M} \sum_{p=1}^M (w_{\text{cor}}^p \cdot \text{IWU}_p), \quad (13)$$

where M is the number of precipitation products ($M = 4$); and w_{cor}^p is the weight for IWU_p , which is derived from the soil water balance status

$$w_{\text{cor}}^p = r_p / \sum_{p=1}^M r_p, \quad (14)$$

where r_p represents the matching level between the precipitation product and the set of soil moisture data, which can be calculated from the correlation between the satellite-based precipitation (P_{obs}) and the derived precipitation (P_{der})

$$r_p = \frac{\text{cov}(P_{\text{der}}, P_{\text{obs}})}{\sigma_{P_{\text{der}}} \cdot \sigma_{P_{\text{obs}}}}, \quad (15)$$

$$P_{\text{der}}(\phi; t) = Z_s \frac{d\theta}{dt} + ET(t) + D(t), \quad (16)$$

where P_{der} is the derived precipitation from the soil water balance equation on irrigation-free days ($I = 0$).

3. Data

To cover the available period for most of the satellite-based soil moisture products, we selected 2011–2018 as the study period. All the data were preprocessed to a daily time series with a uniform spatial resolution of 0.25° .

3.1. Remote Sensing Products

3.1.1. Soil Moisture

Eight kinds of satellite-based soil moisture products were selected in this study: three C-band products from the Advanced SCATterometer (ASCAT) and the Advanced Microwave Scanning Radiometer 2 (AMSR2-LPRM and AMSR2-JAXA); four L-band products from the Soil Moisture Ocean Salinity (SMOS-BEC and SMOS-IC) and the Soil Moisture Active Passive (SMAP-L3 and SMAP-L4) satellite missions; and the merged soil moisture product (the Climate Change Initiative Soil Moisture (CCI SM) product) from the Essential Climate Variables (ECV) program developed by the European Space Agency (ESA), for which version v04.7 of the CCI SM product was selected in this study. All these products provide a spatial resolution of 0.25° , except for the SMAP product, which has a spatial resolution of ~ 9 km. The detailed information for these selected products are provided in Table 2.

3.1.2. Precipitation

Four satellite-based precipitation products were selected in this study (Table 3): the Global Precipitation Climatology Project Daily precipitation data set (GPCP-Daily v1.3), with an original spatial resolution of 1° and a global coverage; the Tropical Rainfall Measuring Mission (TRMM) Multisatellite Precipitation Analysis Level-3 product (TMPA-3B42), which provides daily precipitation data and coverage between 50°S and 50°N ; the

Table 2
Details of the Selected Satellite-Based Soil Moisture Products

Product	Platform	Resolution	Data availability	Reference
ASCAT	MetOp-A/B	0.25°	2007–	Wagner et al. (2013)
AMSR2-LPRM	GCOM W1		2012–	Parinussa et al. (2015)
AMSR2-JAXA				Kim et al. (2015)
SMOS-BEC	SMOS MIRAS		2009–	Font et al. (2013)
SMOS-IC				Fernandez-Moran et al. (2017)
SMAP L3	SMAP	~9 km	2015–	Chan et al. (2018)
SMAP L4				Reichle et al. (2019)
CCI SM	Multisource	0.25°	1978–	Dorigo et al. (2017)

Climate Prediction Center MORPHing technique (CMORPH) product, which is obtained from the data of multiple passive microwave satellites, combined with the motion vector of the Geostationary Meteorological Satellite (GMS) infrared data; and the Precipitation Estimation from Remotely Sensed Information using Artificial Neural Networks (PERSIANN) Climate Data Record (CDR), which is trained based on the brightness temperature from geostationary satellites, with the stage IV hourly precipitation data of the National Centers for Environmental Prediction (NCEP). Both the CMORPH and PERSIANN-CDR products provide a spatial resolution of 0.25° and coverage between 60°S and 60°N.

3.1.3. Vegetation Indices (VI) and Albedo

Both the NDVI and the EVI are needed for the PT-JPL model (Table 1). The NDVI and EVI were obtained from the latest MOD13C1 product (<https://lpdaac.usgs.gov/products/mod13c1v006/>, version 006). The MOD13C1 product provides 16-day composites (cloud-free) with a spatial resolution of 0.05°. The tenth band of the white sky albedo from the latest MCD43C1 product (<https://lpdaac.usgs.gov/products/mcd43c1v006/>, version 006) was used in this study for calculating the land surface net radiation (R_n) in the PT-JPL model (see Section 2.1).

3.2. Meteorological Data and Irrigation Map

The downward shortwave radiation (R_s), air temperature (T_a), and specific humidity (RH) needed for the PT-JPL model (see Section 2.1) were acquired from the Modern-Era Retrospective analysis for Research and Applications Version 2 (MERRA-2, Gelaro et al., 2017) of NASA's Global Modeling and Assimilation Office (GMAO, <https://gmao.gsfc.nasa.gov/>). Furthermore, the latest version (5.0) of the Global Map of Irrigation Areas (GMIA) from the Food and Agriculture Organization (FAO) was used in this study to identify the irrigated areas (see Section 2.2). The GMIA can provide the amount of area equipped for irrigation as the percentage of the total area for each pixel, with a spatial resolution of 5 min (Siebert et al., 2013).

Table 3
Details of the Selected Satellite-Based Precipitation Products

Product	Resolution	Coverage	Data availability	Reference
GPCP-Daily	1°	Global	1996–	Adler et al. (2017)
TMPA 3B42	0.25°	50°S–50°N	1998–	Huffman et al. (2007)
CMORPH	0.25°	60°S–60°N	2002–	Joyce et al. (2004)
PERSIANN-CDR	0.25°	60°S–60°N	1983–	Ashouri et al. (2015)

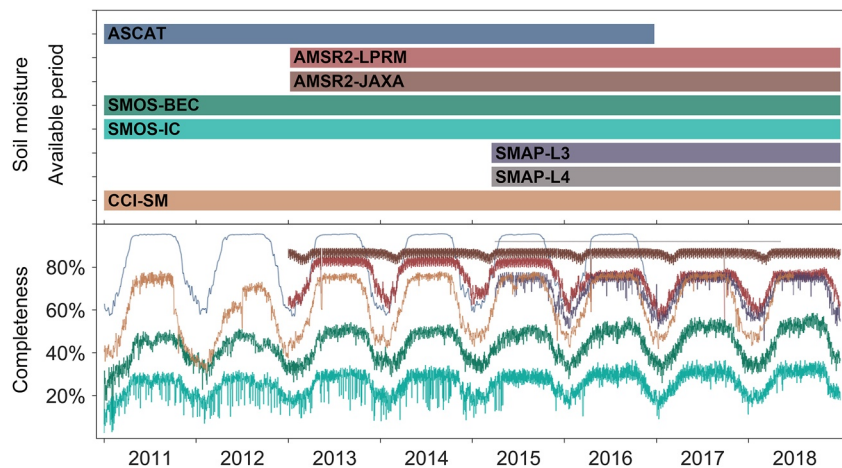


Figure 3. Available periods for the selected satellite-based soil moisture products (upper panel) and their completeness (percentage) for the global irrigated areas.

3.3. Comparison and Validation Data

We used the reported data from the United States Department of Agriculture (USDA; FRIS-2013, the 2013 Farm and Ranch Irrigation Survey), the Chinese Ministry of Water Resources (survey data from 2015), and the FAO (AQUASTAT Report, Irrigation Water Withdrawal by Country) to assess the estimated IWU at different levels (states/provinces/countries). It should be noted that the reported irrigation-related data generally represent the total irrigation water withdrawal (i.e., IWW), rather than the actual IWU. The meanings of the different irrigation-related definitions are explained in Appendix C. We also used the flux data from 12 cropland sites to evaluate the simulated ET, including 11 sites from the FLUXNET2015 data set (<https://fluxnet.org/>) and one site (i.e., the Daman site) from the Heihe Watershed Allied Telemetry Experimental Research (HiWATER) project. Details of these 12 flux sites are provided in Table S1 in Supporting Information S1. We also selected two widely used global ET data sets, i.e., the Global Land Evaporation Amsterdam Model (GLEAM) and the Moderate Resolution Imaging Spectroradiometer (MODIS) ET product (MOD16), to make a comparison with the ET simulation from the coupled PT-JPL model in the IWU estimation. In addition, to test the effect of satellite-based surface soil moisture and site-observed soil moisture when using them to derive the total water input, we used data from 20 flux sites with available site-observed soil moisture and precipitation across different climate zones (Table S2 in Supporting Information S1).

3.4. Data Preprocessing

We counted the valid periods and calculated the data completeness ratio for each soil moisture data set (Figure 3). Specifically, we performed statistical analysis at a daily scale for each soil moisture product, filtering out the valid data (set to 1) and missing data (set to 0) to calculate the overall data completeness ratio for each day. For the spatial resolution, we unified all the input data to a spatial resolution of 0.25° by the use of a nonlinear spatial interpolation method that can eliminate the abrupt boundary changes (Mu et al., 2011). This interpolation method employs a fourth power cosine function to calculate the nonlinear distance from the great circle distance among the four coarse pixels surrounding a given pixel with a targeted resolution (0.25° in this study). The interpolated result for the targeted pixel can then be calculated from the weighted average of the corresponding coarse pixels.

4. Results

4.1. Status of Soil Water Balance

To test the reliability of the proposed method, the key simulated components (i.e., precipitation, ET) in the soil water balance equation were validated against observations. This was based on the hypothesis put forward in

Table 4

Median R Values Computed Between the P_{obs} and P_{der} Derived From the Different Combinations of Soil Moisture and Precipitation Products

	CMORPH	PERSIANN-CDR	TMPA	GPCP
ASCAT	0.83	0.84	0.83	0.83
AMSR2-LPRM	0.80	0.80	0.79	0.79
AMSR2-JAXA	0.79	0.79	0.78	0.79
SMOS-BEC	0.80	0.78	0.78	0.77
SMOS-IC	0.80	0.79	0.79	0.78
SMAP-L3	0.84	0.83	0.83	0.82
SMAP-L4	0.79	0.83	0.81	0.82
CCI SM	0.84	0.84	0.83	0.83
Ensemble ($P_{\text{der}}^{\text{ens}}$)	0.82	0.82	0.81	0.80

$P_{\text{der}}^{\text{ens}}$ estimate (Figure 4c) shows a smaller coverage (50°S–50°N), due to the limited spatial coverage of the TMPA product. The R values show similar spatial distributions for the four cases, and generally remain at a high level ($R > 0.80$) across the vast majority of the global irrigated areas, especially in India, China, and central Continental United States (CONUS). However, relatively low correlations ($R < 0.6$) are found near the equator and the regions around 50°N (e.g., west Russia, northeast US). This can be explained by the following facts. First, soil moisture remains at a high saturation level near the equator regions due to the abundant precipitation and extensive paddy rice cultivation. Second, the topography of these regions (mountainous areas and mixed cropland with forest) is complex, which makes it more difficult for satellites to capture the soil moisture dynamics. Lastly, the soil freeze-thaw processes in the high-latitude regions lead to poor quality for the microwave remote sensing-based soil moisture.

We also validated the ET simulations produced by the coupled PT-JPL model using the flux observations collected at 12 cropland sites (Figure 5). Furthermore, we compared the site observations with two widely used

Section 2.2, i.e., the derived precipitation (P_{der}) using optimized parameters should be well correlated with the satellite-based precipitation (P_{obs}) on rainy days. Table 4 presents the grid-based median values of the Pearson's correlation coefficient (R) computed between the observed P_{obs} and individual P_{der} from the different combinations of soil moisture and precipitation products. The R values range from 0.77 to 0.84, with relatively high R values found for the ASCAT, SMAP-L3, and CCI SM products, due to their relatively high completeness. These results indicate that the optimized parameters perform reasonably well in balancing the soil water dynamics at each pixel. Moreover, the spatial patterns of the optimized parameters are given in Appendix A (Figure A1).

Figure 4 further shows the spatial distributions of the R values computed between the four satellite-based precipitation (P_{obs}) estimates and the corresponding ensemble precipitation estimate ($P_{\text{der}}^{\text{ens}}$), which was calculated from the individual P_{der} estimates of the eight soil moisture products weighted by their completeness ratio. The grid-based median values of the R values between P_{obs} and $P_{\text{der}}^{\text{ens}}$ are also given in Table 4. Noticeably, the TMPA-based

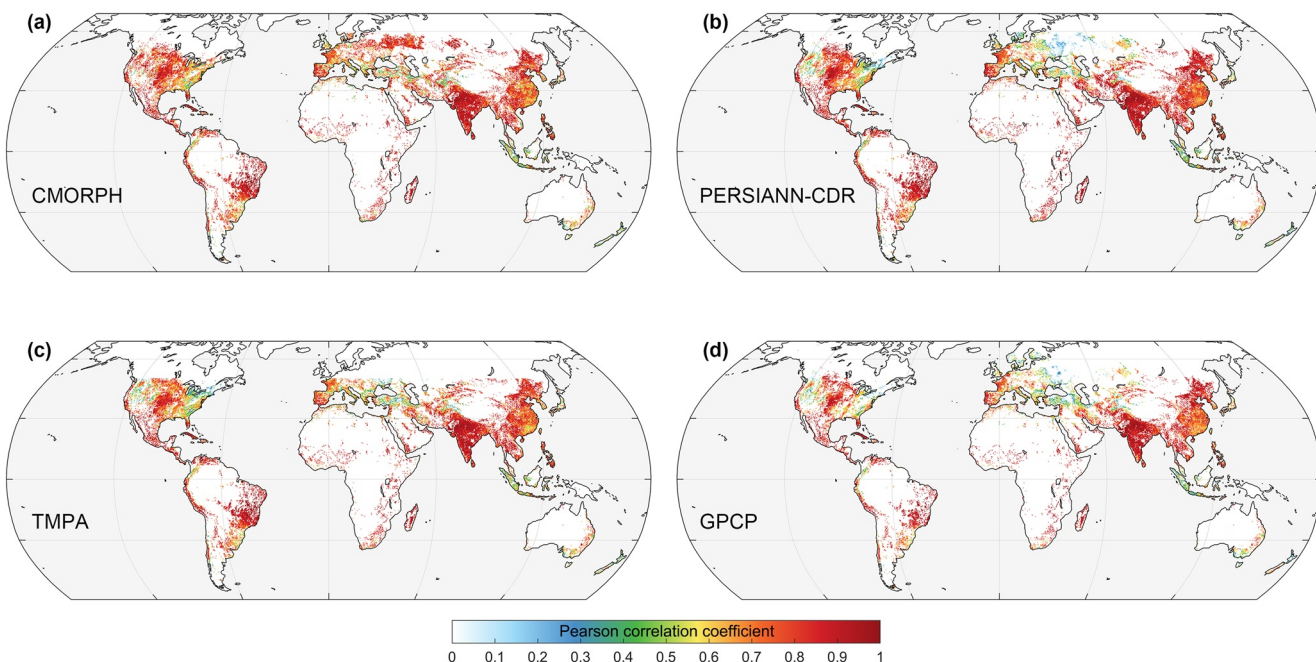


Figure 4. Spatial distribution of the R values between the P_{obs} of the four precipitation products and the corresponding $P_{\text{der}}^{\text{ens}}$ derived from the eight soil moisture products over the global irrigated areas.

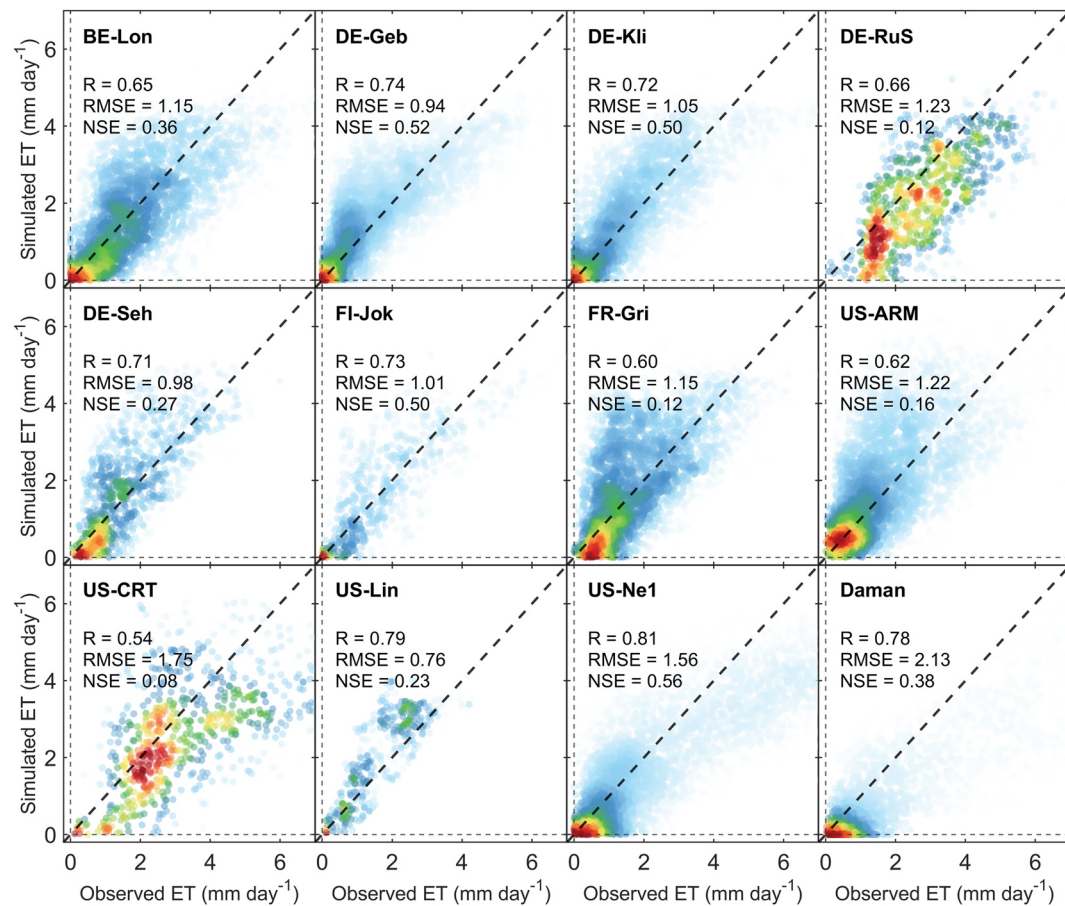


Figure 5. Comparison of the evapotranspiration (ET) simulated by the coupled Priestley-Taylor Jet Propulsion Laboratory (PT-JPL) model used in this study with the observations collected from 12 cropland flux sites (11 sites from the FLUXNET data set and one site from the HiWATER project). For the site-scale test, we used the meteorological data from the flux site combined with the vegetation index from MOD13C1 (spatial resolution of 0.05°) as the forcing data for the PT-JPL model.

ET products, to verify the robustness of the coupled PT-JPL ET scheme (Figure 6 and Figures S2 and S3 in Supporting Information S1). The coupled PT-JPL model exhibits a low root-mean-square error (RMSE) across all the sites ($<2 \text{ mm day}^{-1}$), except for the Daman site in northwest China (RMSE = 2.13 mm day^{-1}), and shows a superior performance with higher R value and Nash-Sutcliffe efficiency (NSE) score than the other two global ET products (Figure 6). These results confirm the effectiveness of the proposed framework in estimating the key components of the soil water balance equation across the global irrigated areas.

4.2. Comparison of the IWU Estimates With the Reported IWW

We compared the estimated IWU_{ens} with the reported IWW from the USDA at the state level, the reported IWW from 31 provinces of China, and the reported IWW from the FAO at the country level (see Section 3.3). Figure 7 shows the regression of the IWU estimates versus the reported IWW for the three selected cases (i.e., the states of the US, the provinces of China, and the countries from the FAO). For the 50 states of the US with well-developed irrigation systems, the estimated IWU_{ens} shows reasonable correlation with the reported data, with the values of R , bias, and RMSE being 0.71, -0.42 km^3 , and 3.24 km^3 , respectively. For the 31 provinces of China, a lower R value (0.50) but higher bias (3.10 km^3) and RMSE (8.95 km^3) are obtained. For the comparison between the IWU estimates and the FAO-reported IWW at the country level, the R value is as high as 0.95, while the bias and RMSE are -10.84 and 40.07 km^3 , respectively. In general, the comparison at the country level shows a higher R value but considerably more bias and RMSE than the comparisons made at the state and province level. The explanation for this could be the large number of statistical points (up to 172 countries) with the larger range of

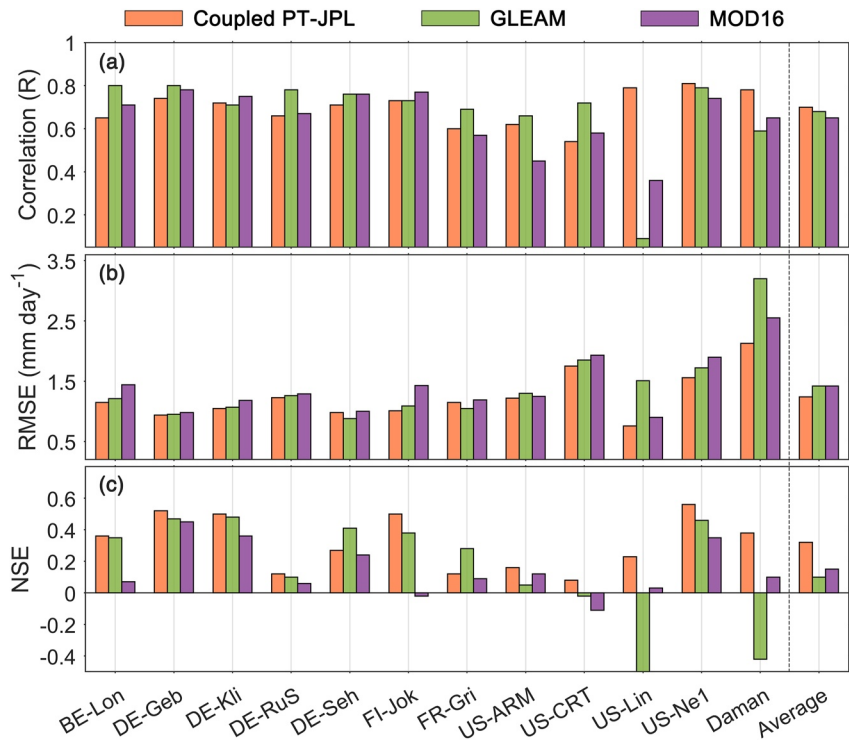


Figure 6. Statistics of the performances of the coupled PT-JPL, GLEAM, and MOD16 models, compared with the flux observations over croplands.

values (i.e., $\sim 688 \text{ km}^3 \text{ year}^{-1}$ for the India IWW) in the country-level comparison. Moreover, we compared our IWU estimates with the latest FRIS2018 survey data at the different states of the US (see Figure S4 in Supporting Information S1), with the values of R , bias, and RMSE being 0.73, -0.70 km^3 , and 3.38 km^3 .

To evaluate the performance of the proposed IWU estimation algorithm at a regional scale, we selected the Heihe River Basin (HRB) and the Shiyang River Basin (SRB), where are two inland river basins in northwest China and the cropland is mainly supplied by irrigation (see Figure S5 in Supporting Information S1). The interannual variation of the estimated IWU exhibits high correlation with the reported data (Figures 8a and 8b), which can indirectly verify the accuracy of IWU estimates if the conveyance efficiency (E_c) remains stable during the study period. In addition, we selected an extreme arid irrigated area in the Kingdom of Saudi Arabia, where agricultural

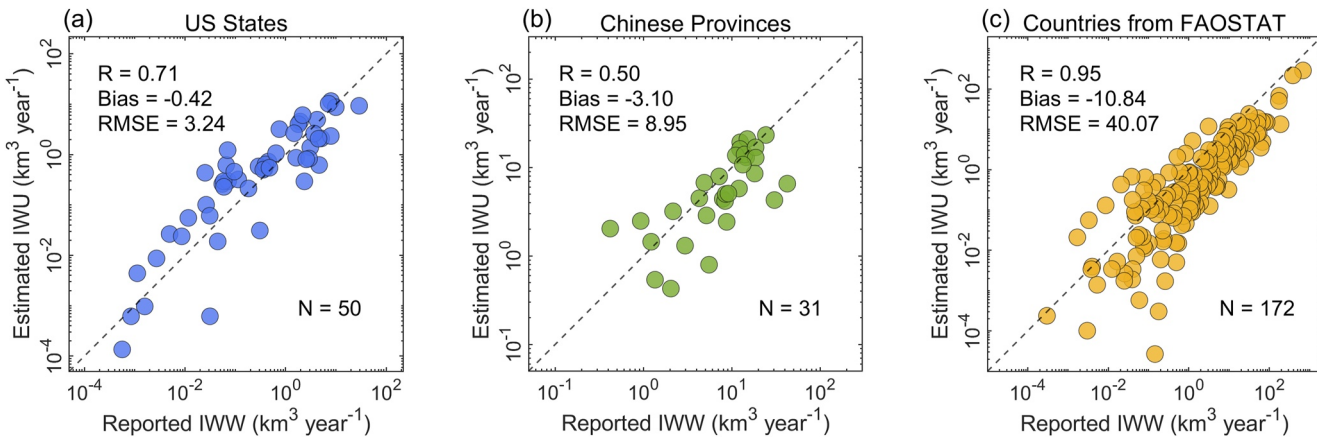


Figure 7. Comparisons of the ensemble mean irrigation water use (IWU_{ens}) estimates with the reported irrigation water withdrawal (IWW) in: (a) 50 states of the US, (b) 31 provinces of China, and (c) 172 countries with the IWW above 5 km^3 from the Food and Agriculture Organization (FAO).

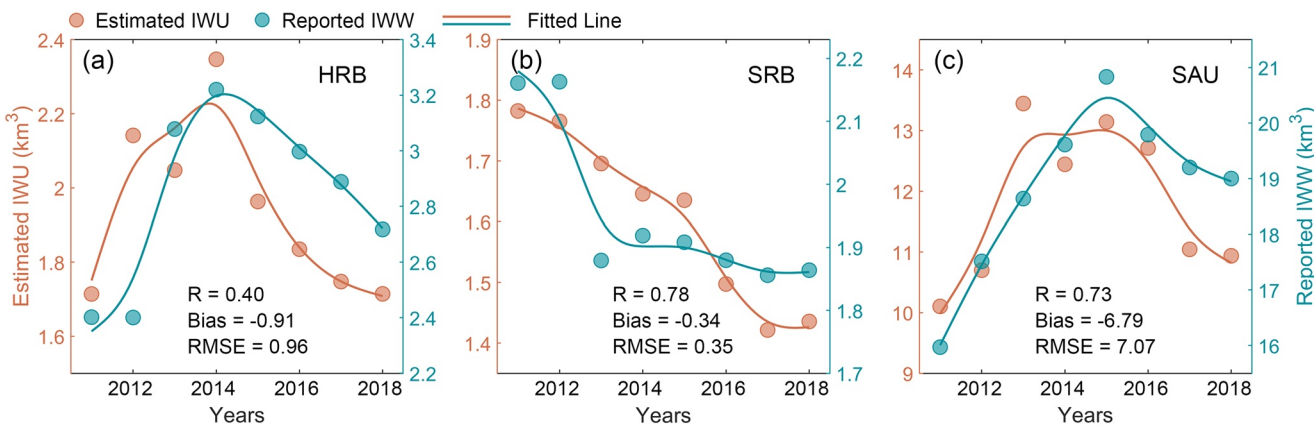


Figure 8. Comparison between the estimated irrigation water use (IWU) and reported data for (a) Heihe River Basin (HRB), (b) Shiyang River Basin (SRB), and (c) the Kingdom of Saudi Arabia (SAU). The reported irrigation water withdrawals were derived from the annual report on water resources of Gansu Province (China) and the 2019 statistical yearbook from the Ministry of Environment Water & Agriculture of the Kingdom of Saudi Arabia.

irrigation is mostly dependent on groundwater (see Figure S6 in Supporting Information S1). Similarly, the estimated IWU are generally consistent with the reported data ($R = 0.73$, Figure 8c). Thus, these results indicates that the proposed IWU estimation scheme can capture the dynamic changes of irrigation at regional scale and also exhibit reasonable application performance in the groundwater supply regions.

Figure 9 further shows an intracomparison of the RMSE for the different kinds of IWU estimates obtained in this study, including the simple average of the 32 individual IWU_i estimates (gray lines) and its corresponding range for the different precipitation products (see the boxplot in Figure 9), the four kinds of IWU_p (blue diamonds) and their simple mean result (IWU_{avg}^p , blue lines), and the final IWU_{ens} (green lines). The IWU_i shows considerable uncertainty across the different comparison levels, and the corresponding mean RMSE of IWU_i is relatively high across the different cases (4.2 km^3 for the US states, 11.3 km^3 for the Chinese provinces, and 54.5 km^3 for the FAO countries). On the other hand, the RMSE of the IWU_{ens} (green lines) remains around an acceptable level (relatively low) across the different cases (US, China, and FAO), which indicates that the IWU_{ens} is the

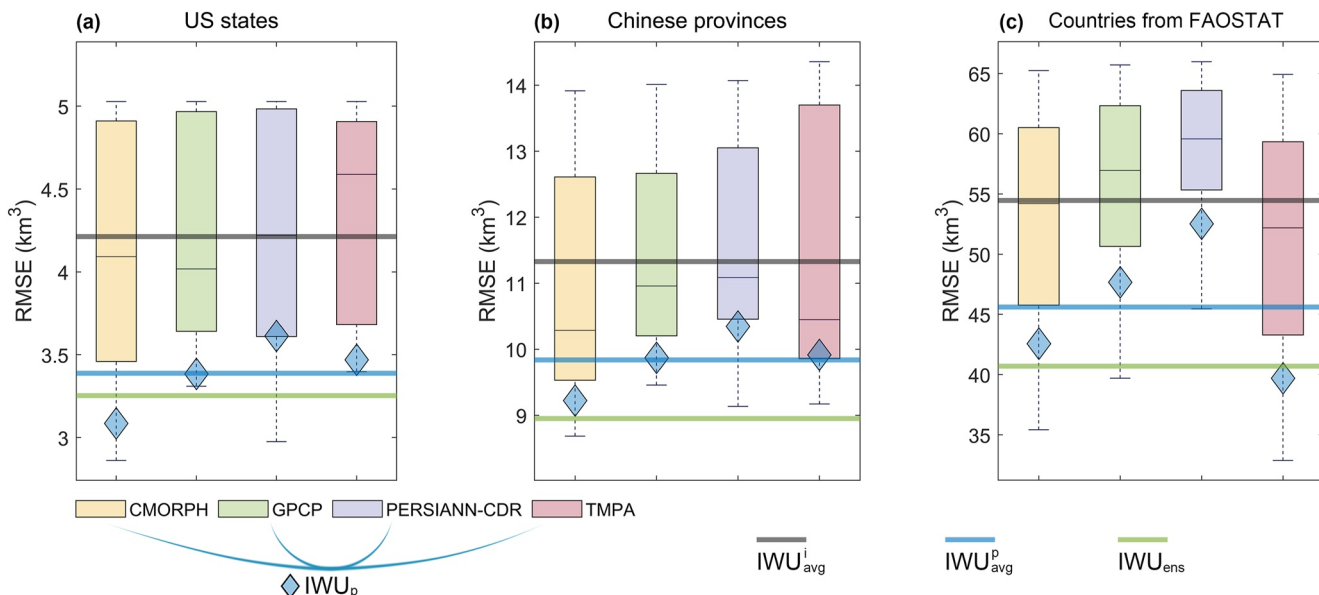


Figure 9. Comparison of the root-mean-square error (RMSE) of the different irrigation water use (IWU) estimates from the 32 individual IWU_i estimates grouped for the different precipitation products (boxplot) and their average results (IWU_{avg}^i), the weighted IWU results for the four kinds of precipitation products (IWU_p) and their simple mean results (IWU_{avg}^p), and the ensemble results (IWU_{ens}).

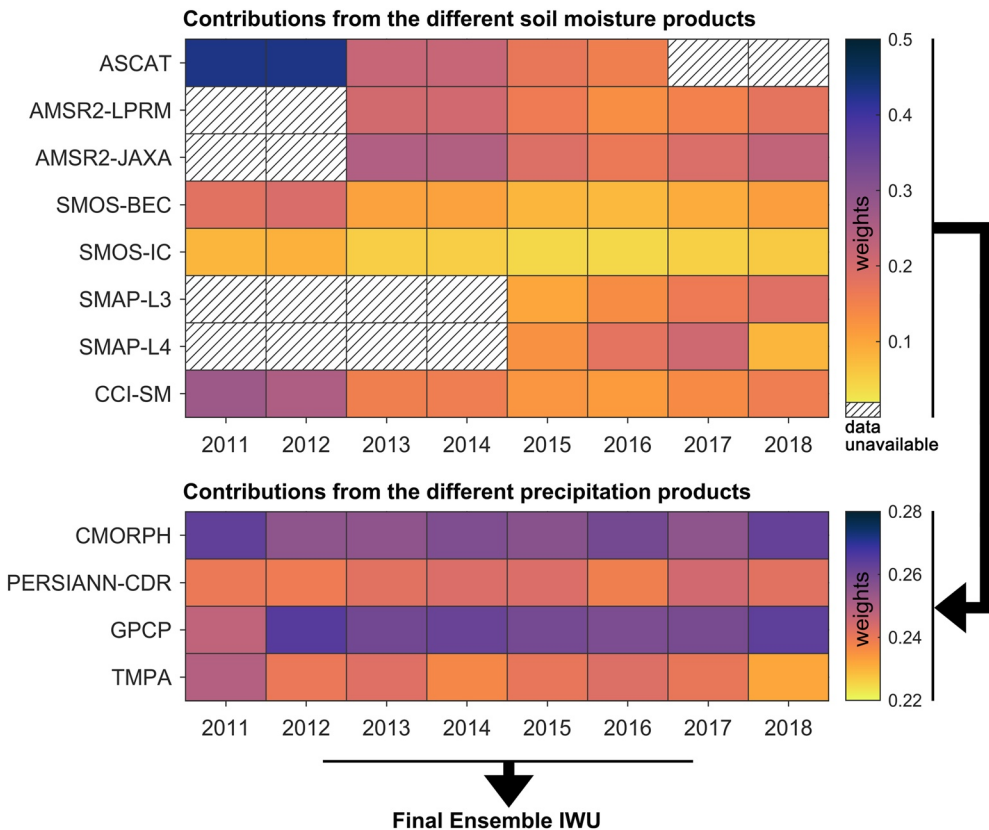


Figure 10. The different contributions of the multiple satellite-based products to the final ensemble irrigation water use (IWU_{ens}) estimates.

most reliable and robust result among all the kinds of estimated IWU (Figure 9). Although the CMORPH-based IWU (IWU_{CMORPH}) and TMPA-based IWU (IWU_{TMPA}) perform better in the US states ($RMSE = 3.08 \text{ km}^3$, IWU_{CMORPH}) and FAO countries ($RMSE = 39.69 \text{ km}^3$, IWU_{TMPA}), the integrated IWU_{ens} results show a better performance at the various scales.

In addition, since the integrated IWU_{ens} is derived from the weighted average of the different precipitation and soil moisture products, we can quantify their respective contributions from their corresponding weights. From Figure 10, we can see that ASCAT, AMSR2-JAXA, and CCI SM have the most impact on the IWU_{ens} . In contrast, the soil moisture products from SMOS (including the IC and BEC products) make a relatively low contribution to the IWU_{ens} . For the different precipitation products, CMORPH and GPCP have relatively large weights when compared with PERSIANN-CDR and TMPA. It should be noted that a twill box indicates that there are no data in the specific year.

4.3. Spatial and Temporal Patterns of the Global IWU Estimates

Figure 11 shows the spatial distribution of the annual mean IWU_{ens} from 2011 to 2018. Notably, the maximum IWU values are found in the northern parts of Pakistan (i.e., the Indus River Basin) and India (i.e., the Ganges River Basin), where the world's largest irrigation systems are found. In East Asia, a relatively high IWU value is found in the North China Plain, which is the main grain-growing region of China. For the US, the major irrigation water contributors are found in California, the Mississippi Valley, and the Central Great Plains. In Europe, the IWU is mainly concentrated in the Iberian and Apennine peninsulas. The distribution of the IWU is very sparse in the Southern Hemisphere, and is more concentrated in limited regions of Australia and southern Chile. In addition, the spatial distribution of the four kinds of IWU_p estimates is shown in Appendix B (Figure B1).

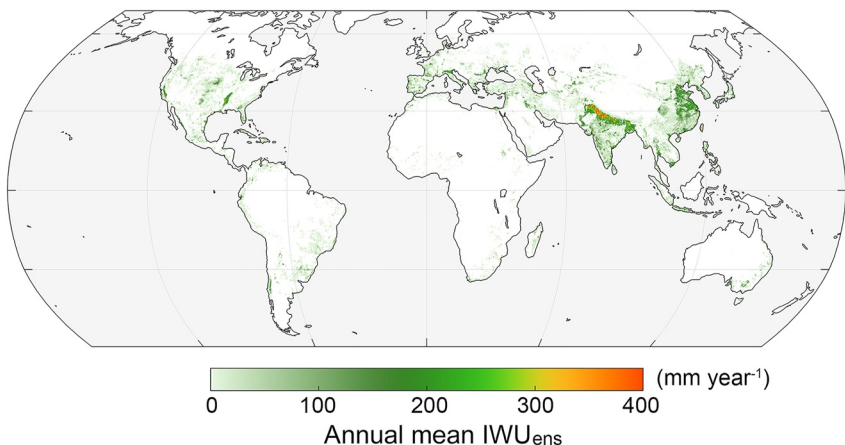


Figure 11. Spatial distributions of the ensemble mean annual irrigation water use (IWU) from 2011 to 2018.

Overall, the total amount of global annual IWU is about $959 \pm 130 \text{ km}^3 \text{ year}^{-1}$, based on the IWU_{ens} estimates for the period of 2011–2018. Figure 12 further shows the statistics for the irrigated area and IWU_{ens} for the top 12 major irrigated countries/regions in the world. The top 12 countries/regions account for about 75% of the global irrigated area and about 81% of the global IWU. Among these countries/regions, India and China have the most irrigated land (21% and 20% of the global irrigated area, respectively), and account for 25% and 23.8% of the global IWU, respectively. Moreover, the IWU changes of India and China make a contribution of at least 8% to the change of global IWU during the study period of 2011–2018 (error bar in Figure 12). The US is the third-largest contributor, and accounts for about 9.3% of the global irrigated area and 8.3% of the global IWU.

To explore the IWU variation and its link to hydrological cycling, we compared the monthly IWU anomalies, as well as the ET and precipitation anomalies, around the world and the top five irrigated countries/regions for the period of 2011–2018 (Figure 13). An upward tendency can be observed for the monthly anomalies of global IWU (Figure 13a) from September 2012 to September 2013, which is followed by a general declining trend for the rest of the study period. A similar phenomenon can also be observed for the five selected countries/regions. Furthermore, relatively high consistency between the monthly anomalies of IWU and ET can be found in India and Pakistan (Figures 13b and 13f), especially after 2016. However, the correlation between the monthly anomalies of IWU and ET is relatively low in China, the US, and the EU (Figures 13c, 13d, and 13e), while the precipitation shows more relevance to ET. Further study to explore the linkages between the different hydrological components is still needed.

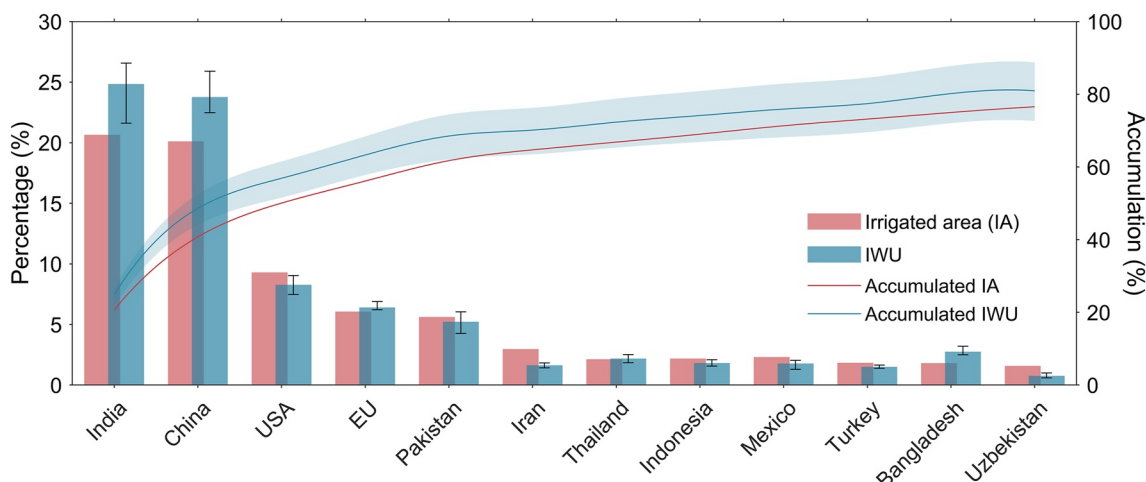


Figure 12. Statistics for the irrigated area and mean annual (IWU) for the top 12 irrigated countries/regions from 2011 to 2018. The irrigated area was calculated from the Global Map of Irrigation Areas (GMIA) product in this study. The error bars represent the range of the IWU estimates during the period from 2011 to 2018.

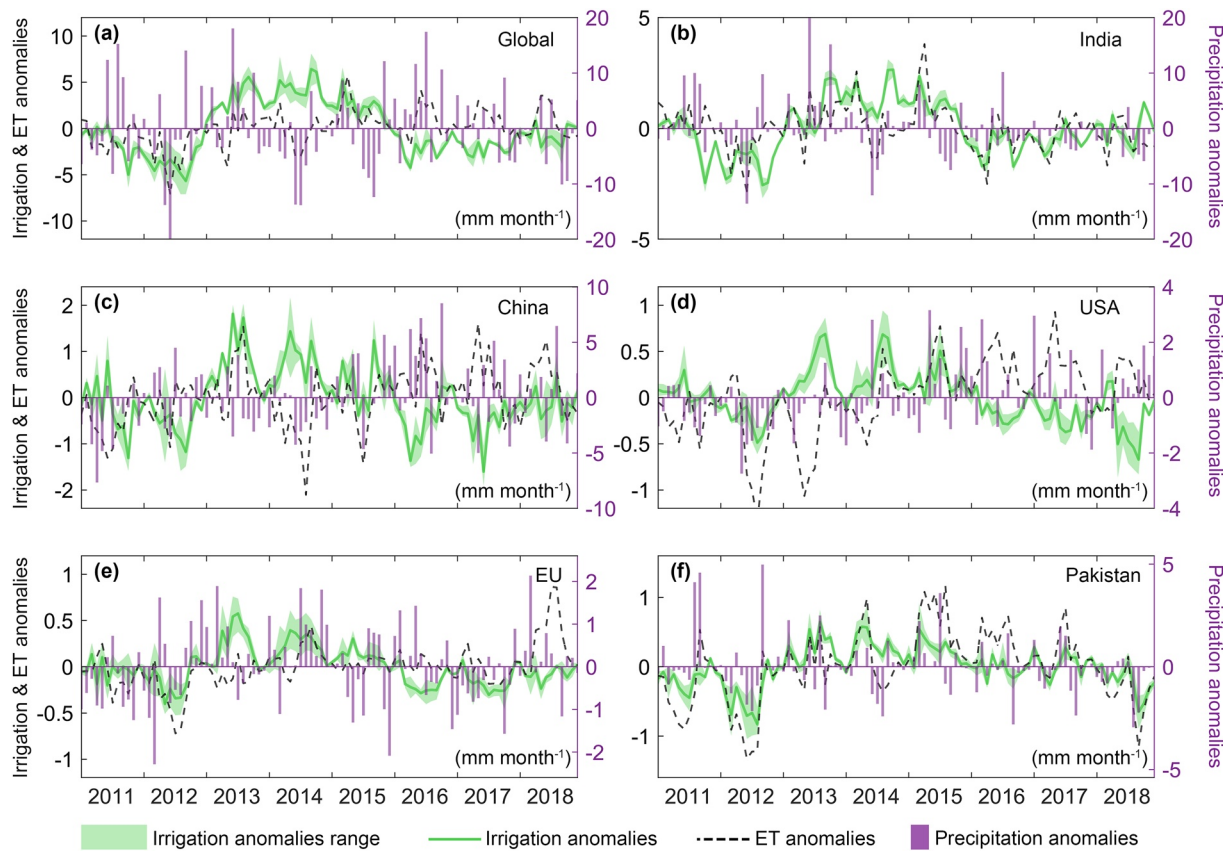


Figure 13. Monthly anomalies of irrigation water use (IWU), evapotranspiration (ET), and precipitation around the world and the top five primary irrigated countries/regions from 2011 to 2018. The bar plots in purple and the black dotted lines represent the precipitation and ET anomalies, respectively. The green lines and ranges represent the anomalies from the IWU_{ens} and four kinds of IWU_p, respectively.

5. Discussion

Theoretically, the rapid increase in soil moisture observed by satellite on rain-free days can be mainly attributed to irrigation, and can thus be used to estimate IWU. This principle has been widely used for the estimation of IWU at local scales in previous studies (Brocca et al., 2018; Dari et al., 2020; Filippucci et al., 2020; Jalilvand et al., 2019). This “bottom to up” approach focuses on the changes in the soil water balance to estimate IWU, which skillfully avoids the uncertainties and unpredictability of irrigation events caused by human behavior. However, the accuracy in estimating IWU at a global scale depends on the proper parameter values in the algorithm, accurate quantification of ET, and the completeness of the satellite-based data. In this paper, we have proposed a framework that couples the soil water balance equation with optimized parameters and the PT-JPL model to estimate global IWU by integrating multiple satellite-based products (eight soil moisture products and four precipitation products).

The parameters (e.g., Z_s and K_s) are critical when determining the capacity of soil to hold and leak water. Although microwave sensors can only detect soil moisture in a limited depth range (Zheng et al., 2019), the optimized parameters in combination with satellite-based surface soil moisture estimations can be used to obtain proper estimates of soil water content. Thus, reasonable estimates of the recharge of water into soil due to precipitation or irrigation can also be obtained. The results obtained in this study indicate that the spatial distributions of the optimized parameters are reasonable and consistent with the climate and land surface conditions (Figure A1). A good agreement is also seen between the satellite-based precipitation and derived precipitation over most of the irrigated areas around the world (Figure 4). To further confirm our judgment, we compared the in situ observed precipitation and derived precipitation using satellite-based (P_{der}^{sat}) and in situ observed (P_{der}^{sit}) soil moisture at 20 flux sites. The results show that both kinds of derived precipitation vary consistently with the in situ observed precipitation (Figure S7 and Table S2 in Supporting Information S1). Hence, we can conclude that the DE-MC

Table 5*Comparison of the Error Statistics Between the IWU Estimates Obtained in This Study and Those of Previous Studies*

	R		Bias ($\text{km}^3 \text{ year}^{-1}$)		RMSE ($\text{km}^3 \text{ year}^{-1}$)	
	This study	Previous study	This study	Previous study	This study	Previous study
US states	0.71	0.36–0.80	−0.42	−2.47 to −2.29	3.24	5.21–5.32
FAO countries	0.96	0.72–0.81	−65.8	−76.6 to −73.9	104.1	81.8–97.7

Note. The previous statistics for the US states are from Zaussinger et al. (2019); the previous statistics for the FAO countries are from Zohaib and Choi (2020). It should be noted that we selected the countries from the FAO with an annual IWW of above 20 km^3 , to ensure the same comparison level as Zohaib and Choi (2020).

scheme can be used to successfully identify the optimal parameter values from their prior distributions and satellite observations.

Moreover, the ET process is critical in determining the soil water dynamics (Siebert & Döll, 2010), and further influences the accurate estimation of global IWU. In addition to the effect of soil moisture, ET is highly correlated with plant biophysical characteristics, such as the canopy conductance and vegetation greening (Ma et al., 2021; Schlesinger & Jasechko, 2014; Wei et al., 2017). Previous studies have illustrated that the PT-JPL model can obtain good performances in simulating ET over different land surface conditions (Michel et al., 2016; Zhang et al., 2017). The findings of our study indicate that the coupled PT-JPL model can provide a better ET estimation for cropland than the other global ET products (Figures 5 and 6). Furthermore, we replaced the ET estimated by the PT-JPL model with two widely used ET products (GLEAM and MOD16) and recalculated the final IWU_{ens} (see Figure S8 in Supporting Information S1). The results of this comparison (i.e., bias, RMSE, and NSE) fully demonstrate the advantage of the coupled PT-JPL model for global IWU estimation.

Another critical problem when estimating global IWU is the completeness of the soil moisture data, which are often subject to the data gaps caused by the discontinuous satellite coverage and revisit frequency (Wang et al., 2012). To overcome this problem, we have proposed a framework to integrate the different kinds of soil moisture and precipitation products and properly estimate global IWU. The results indicate that the ensemble IWU (IWU_{ens}) estimates are reasonable when compared to the reported data from the states/provinces of the US and China. In addition, the IWU_{ens} provides a more robust estimate than the $\text{IWU}_{\text{avg}}^i$ and $\text{IWU}_{\text{avg}}^p$ (Figure 9), which indicates that the ensemble scheme is effective in reducing the uncertainty in estimating global IWU. When comparing the results of this study to the results reported in previous studies (Zaussinger et al., 2019; Zohaib & Choi, 2020), it can be found that the method proposed in this paper is generally better in estimating IWU. As demonstrated in Table 5, Zaussinger et al. (2019) compared their IWU estimates with the 2013 FRIS report of the USDA, and the obtained bias ranged from −2.47 to −2.29 km^3 . Zohaib and Choi (2020) compared their IWU estimates with the FAO statistical data across different countries, and the obtained bias ranged from −76.6 to −73.9 km^3 . In addition, we further compared our IWU estimates in the CONUS with recent irrigation-related studies (Chen et al., 2019; Zhang & Long, 2021) based on 2013/2018 FRIS data, and good agreements among them were found (see Figure S9 in Supporting Information S1).

Nevertheless, an underestimation in IWU can be observed in the results of the current study (see Section 4.2). This phenomenon has also been reported in previous studies (e.g., Jalilvand et al., 2019; Zaussinger et al., 2019; Zohaib & Choi, 2020), and can be explained by the following reasons. First, the spatial resolution of the soil moisture products (~25 km) is too coarse to capture some of the changes in soil moisture within a complex pixel, especially when the irrigated area only accounts for a small fraction of a pixel. Thus, it is difficult for the satellite to identify the slight changes in soil moisture caused by irrigation. This issue is well known as the “scale effect,” in that satellite-based observation is the composite retrieval of information within a single pixel (Cao et al., 2020). Fortunately, new advances in satellite sensors/missions (e.g., ECOSTRESS; Fisher et al., 2020) can be expected to help solve the problem and promote IWU estimation at a finer spatial resolution. Besides, the inconsistency between precipitation and soil moisture data can also affect the identification of irrigation signals, which leads to spurious irrigation.

Furthermore, the reported irrigation data are usually the IWW statistics without considering the conveyance efficiency (E_c). However, it is challenging to obtain E_c at the pixel scale as it is commonly affected by the soil

Table 6

Intercomparison of the Main Statistics Between the Estimated IWU, the Original IWW, and the Modified IWW Considering Conveyance Efficiency

Original IWW	Modified IWW ^a				
	Case 1	Case 2	Case 3	Case 4	
Bias ($\text{km}^3 \text{ year}^{-1}$)	-10.84	-5.86	-6.69	-7.52	-10.01
RMSE ($\text{km}^3 \text{ year}^{-1}$)	40.07	20.85	23.94	27.13	36.81

^aCase 1: open canal with sand lining ($E_c = 0.70$); Case 2: open canal with loam lining ($E_c = 0.75$); Case 3: open canal with clay lining ($E_c = 0.80$); Case 4: pipe canal for sprinkler and drip technology ($E_c = 0.95$).

texture/type (seepage and percolation), the physical condition of the irrigation waterway (e.g., cracks and pipeline aging), and the atmospheric environment (surface evaporation). To make the IWW statistics more comparable to the estimated IWU, we conducted a sensitivity experiment with different values of E_c for the reported IWW statistics, based on a previous study (Jägermeyr et al., 2015), and then conducted an intercomparison between the estimated IWU_{ens} , the original IWW, and the modified IWW at the FAO country level (Table 6). The underestimation of IWU is improved by the modified IWW that considers the conveyance efficiency. Especially in Case 1 (open canal with sand lining, $E_c = 0.70$), the RMSE is improved by about 47.9% relative to the original IWW. Hence, the uncertainty caused by the differences in the concepts of IWW and IWU should not be ignored (see Appendix C).

It should also be noted that the irrigated areas used in the current study are static rather than dynamic, which can also cause some underestimation of IWU in regions with rapid irrigation expansion. For instance, as the most significant contributor to the IWU of China, the irrigated areas in Xinjiang have expanded greatly during the period between 2011 and 2018 (see Figure S10 and Table S3 in Supporting Information S1), which somewhat explains the underestimation of the IWU in this region. Lastly, the soil moisture is generally saturated in irrigated areas planted with paddy rice or other semiaquatic crops, which makes it difficult to identify the irrigation signal due to the failure in detecting the irrigation signal from the soil moisture data (Ozdogan & Gutman, 2008).

Another disadvantage of the proposed IWU algorithm is that it is difficult to distinguish the contributions from groundwater and surface water to irrigation. An assessment of the implication of the IWU source could be beneficial to the optimal development of groundwater and the exploration of irrigation-climate feedback (Famiglietti et al., 2011). Instead of using a statistical ratio from the inventory of the irrigation regime, satellite gravimetry has recently provided us with a potential way to partition the total IWU in combination with a land surface model (e.g., the Community Land Model; Lawrence et al., 2019), which is an approach that could allow us to monitor water availability at a continuous spatial coverage (Anderson et al., 2015). In addition, crop/plant modeling is also essential to quantify IWC from the point of view of blue water resources (Chen et al., 2019). Much potential progress could be achieved by coupling the satellite-based IWU algorithm and crop models to explore the net/total irrigation efficiency, return flow, and the redistribution of water resources by irrigation.

6. Conclusions

In this paper, to generate an estimation of global IWU, we have proposed an integrated framework to couple the processes associated with irrigation by integrating a total of 32 combinations of satellite-based soil moisture and precipitation products. The PT-JPL model and DE-MC scheme were incorporated into the IWU estimation algorithm to enhance the characterization of the ET process and parameter optimization. The results showed that the ensemble scheme of the proposed framework is a feasible way to improve the accuracy of global IWU estimation. The ensemble scheme also demonstrated lower uncertainty than the IWU estimates from individual satellite observations. The estimated IWU showed a reasonable correlation with the survey-based IWW at different spatial scales (regional level, state/province level, and country level), especially when the reported IWW was modified to consider the impact of conveyance efficiency. In addition, incorporation of the coupled process-based PT-JPL model provided better ET estimation in cropland areas than the other global ET products (GLEAM and MOD16). Our results showed that large amounts of IWU are found in the northern parts of Pakistan and India, North China, California, the Mississippi Valley, the Central Great Plains of the US, and the Iberian and Apennine peninsulas of Europe. These five countries/regions together contribute >70% of the global IWU.

A general underestimation was found when estimating the IWU based on satellite observations, both in this study and previous studies, in comparison to the reported IWW. The main reasons for this can be attributed to the different meanings of IWU and IWW, the coarse spatial resolution of satellite observations, the underestimation of irrigated areas when using a static map, and the deficiency of soil moisture products in detecting irrigation events in irrigated areas planted with paddy rice or other semiaquatic crops. Nevertheless, the framework proposed in this paper has demonstrated advantages in integrating multiple precipitation and soil moisture products, to address the

uncertainties in estimating global IWU, leading to improved IWU estimation when compared to previous studies. Furthermore, as a vital supplement to the traditional survey-based IWU estimates, the global IWU estimates obtained in this study represent an opportunity to assess the impact of human activities in regulating natural water resources. However, continuous efforts are still needed to enhance the satellite sensors and retrieval algorithms, to provide soil moisture and precipitation products with a higher spatiotemporal resolution, and further reduce the uncertainty in estimating global IWU.

Appendix A: Spatial Distribution of Optimized Parameters

The average optimized values and the corresponding standard deviations of the optimized parameters (i.e., Z_s , K_s , b) obtained by the DE-MC scheme are shown in Figure A1. The obtained values for the optimized parameters show reasonable spatial distributions that generally follow the climate and land conditions. For instance, parameter Z_s shows higher values in humid areas (e.g., Southern India, China, and the US) than in arid areas, indicating that the soil column has a stronger capacity for holding water in humid areas.

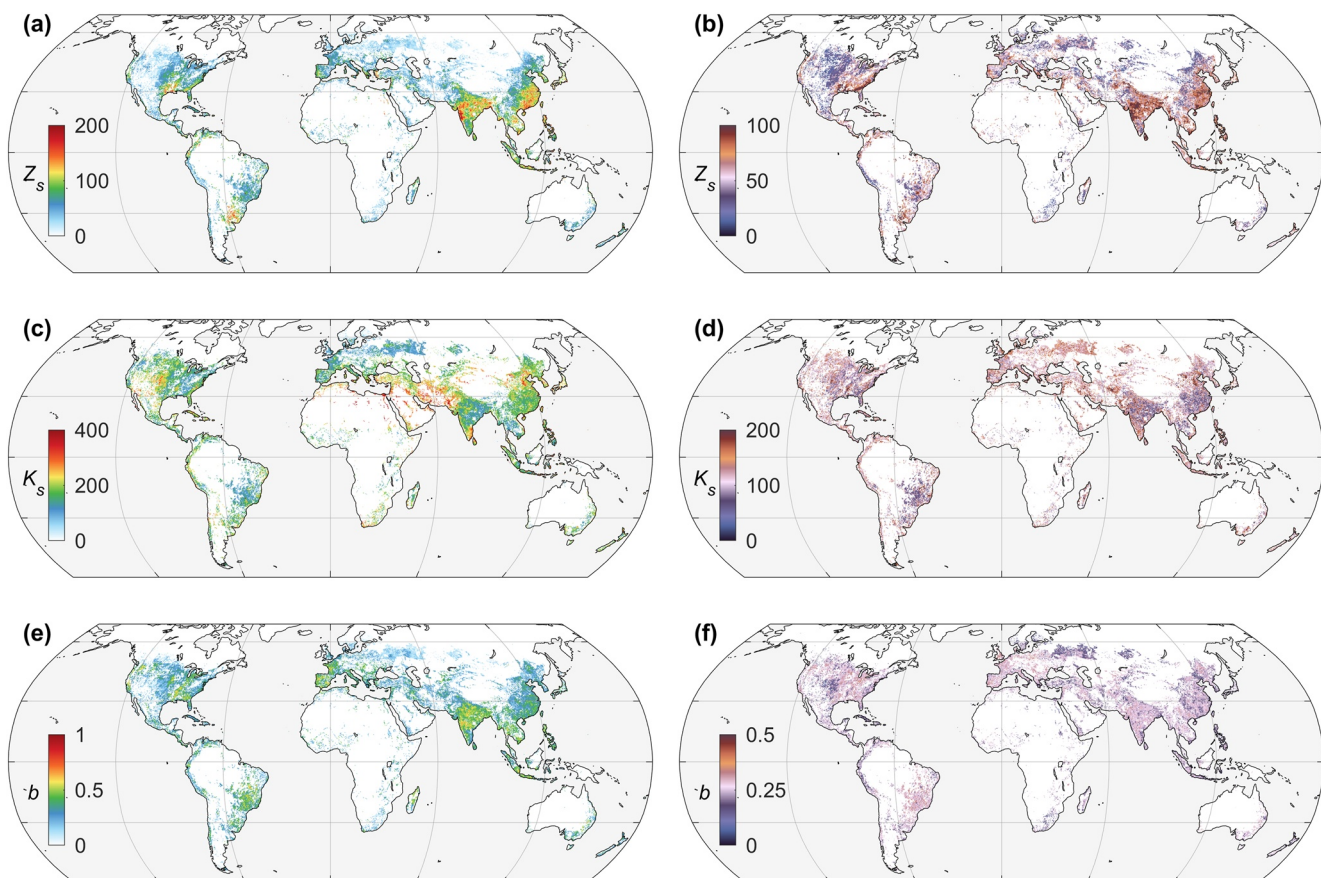


Figure A1. Spatial distribution of the optimized parameters over the global irrigated areas. (a), (c), and (e) represent the average values of optimized parameters Z_s , K_s , and b ; (b), (d), and (f) represent the corresponding standard deviation (std) obtained by the differential evolution Markov chain (DE-MC) scheme.

Appendix B: Spatial Pattern of the Global IWU Estimates Obtained With Different Precipitation Products

The spatial differences in the IWU estimates obtained using different precipitation products as the target are illustrated in Figure B1. The different IWU_p estimates (i.e., $\text{IWU}_{\text{CMORPH}}$, IWU_{TMPA} , $\text{IWU}_{\text{PERSIANN-CDR}}$, IWU_{GPCP}) generally show comparable spatial distributions, whereby the magnitudes of $\text{IWU}_{\text{CMORPH}}$ and IWU_{TMPA} are larger than those of $\text{IWU}_{\text{PERSIANN-CDR}}$ and IWU_{GPCP} . Among the different products, the $\text{IWU}_{\text{PERSIANN-CDR}}$ estimates are clearly lower than the others in both China and India.

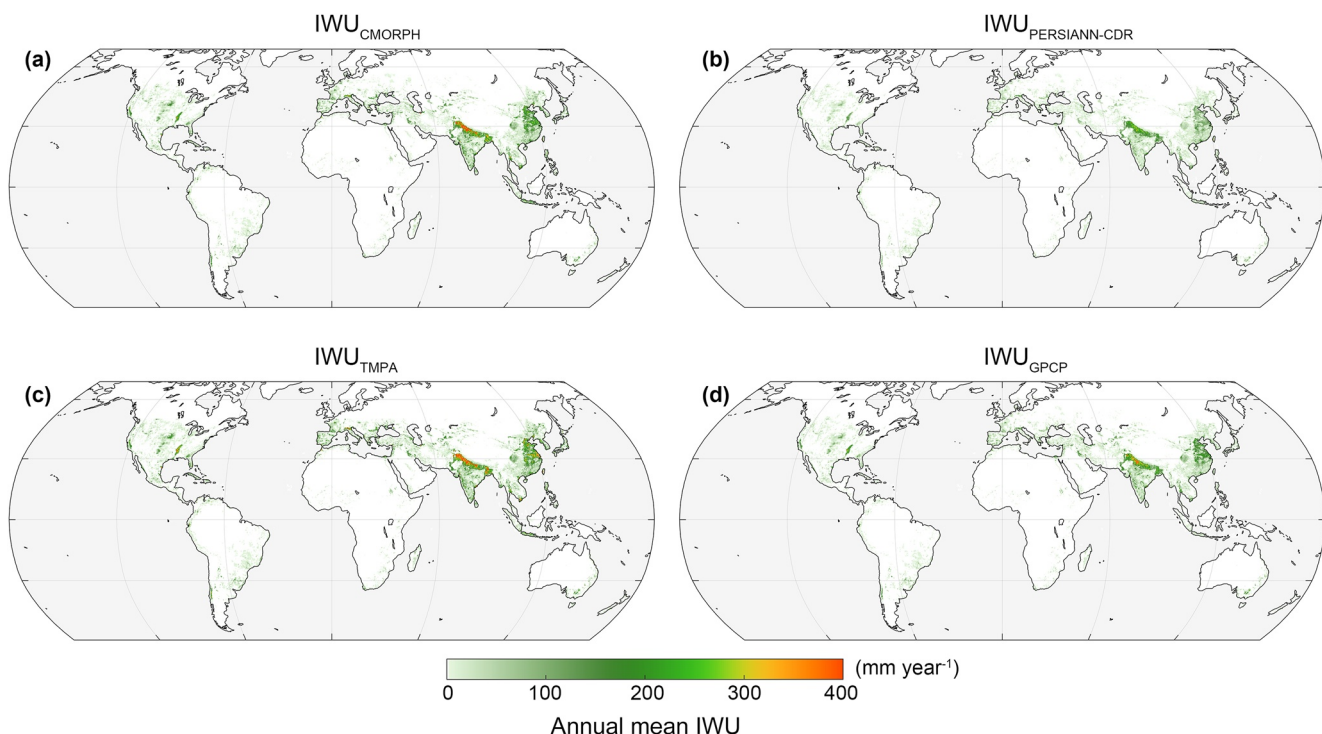


Figure B1. Spatial distributions of the mean global annual IWU_p estimates produced based on the four different precipitation products from 2011 to 2018.

Appendix C: Different Irrigation-Related Definitions

There are several different irrigation-related definitions that need to be clarified:

1. Irrigation water withdrawal (IWW) represents the total water amount diverted from the water source (e.g., surface river or groundwater well). The IWW is also the only irrigation water data that can be directly recorded by water management sectors. However, it is usually counted at the scale of a whole irrigated area (or administrative division), rather than at the field scale.
2. IWU, which was estimated in this study, represents the actual water amount entering into the field. Generally speaking, IWU is less than IWW, to some extent, depending on the conveyance efficiency (E_c) of the irrigation waterway from the water source to the irrigated field. E_c varies greatly in space, and is usually high in developed countries, but can be very low in developing countries. For example, the irrigation water in Kansas in the US is pumped and carried in closed conduits, so that the E_c should be nearly 100% in consequence (Rogers, 1997), whereas the E_c can be around 50% in open canals without lining, in some arid regions such as central Asia.
3. Irrigation water requirement (IWR) is defined as the quantity of water required to support healthy crop growth, and specifically to satisfy transpiration. In nonirrigated areas, precipitation is the only way to satisfy plant water requirement, while irrigation is used to compensate for the transpiration deficit in irrigated environments. Furthermore, the IWC is defined as the actual irrigation water used by crops (also known as the blue water consumption), which should be less than or equal to the IWR. Thus, for a specific crop type, the IWR/IWC is a complex variable, which is dependent on precipitation and the plant physiological condition during the growing season. Hence, IWR/IWC will be close to IWU when the water application efficiency is high (e.g., trickle irrigation); otherwise, IWR/IWC will be much lower than IWU, in most cases.
4. The overall irrigation water efficiency (E_o) represents the effectiveness of the irrigation system, and is expressed as the ratio of irrigation water stored in the root zone (can be used by crops, approximately equal to IWC) to that withdrawn from water sources (Li et al., 2020). E_o can also be the product of the conveyance efficiency (E_c) and the water application efficiency (E_a). Here, E_a is expressed as the ratio of irrigation water stored in the root zone to that irrigation water actually entering the field (IWU). Therefore, E_o should be generally lower than E_c or E_a .

Data Availability Statement

The MODIS products are available from the Land Processes Distributed Active Archive Center (LPDAAC) at <https://lpdaac.usgs.gov/>. The meteorological data from MERRA-2 are available from the Goddard Earth Sciences Data and Information Services Center (GESDISC) at <https://disc.gsfc.nasa.gov/>. The global map of irrigated area from Food and Agriculture Organization is available at <http://www.fao.org/aquastat/en/>. The flux data used in this study are achieved from FLUXNET2015 at <https://fluxnet.org/> and HiWATER at <https://data.tpdc.ac.cn/en/>. The satellite-based soil moisture data of the ASCAT are available from the Integrated Climate Data Center (ICDC) at <https://icdc.cen.uni-hamburg.de/en/>; the AMSR2 are available from GESDISC at <https://disc.gsfc.nasa.gov/>; the SMAP are available from National Snow and Ice Data Center (NSIDC) at <https://nsidc.org/>; the SMOS-BEC are available from the Barcelona Expert Center at <http://bec.icm.csic.es/>; the SMOS-IC are available from the Centre Aval de Traitement des Données SMOS (CATDS) at <https://www.catds.fr/>; the ESA-CCI are available from ESA at <https://esa-soilmoisture-cci.org/>. The satellite-based precipitation data of the GPCP, CMORPH, and PERSIANN-CDR are available from National Center for Atmospheric Research (NCAR) at <https://climatedataguide.ucar.edu/climate-data>; the TMPA-3B42 are available from GESDISC at <https://disc.gsfc.nasa.gov/>. The generated IWU data in this study can be achieved from National Tibetan Plateau Data Center (TPDC) at <https://doi.org/10.11888/hydro.tpdc.271220>.

Acknowledgments

The authors gratefully acknowledge the support from the National Natural Science Foundation of China (Grant Nos. 41901381 and 41988101), the Strategic Priority Research Program of the Chinese Academy of Sciences (Grant No. XDA20100104), and the China Postdoctoral Science Foundation (Grant No. 2019M660815). We would like to thank Bin Cao, Yushan Zhou, Yunquan Wang, and Chunjie Gu for their valuable suggestions in paper preparation and data processing. We also thank Caijin Zhang for providing the comparison data. We are grateful to the principal investigators and their teams for all the data sets used in this study.

References

- Adler, R., Wang, J.-J., Sapiano, M., Huffman, G., Bolvin, D., Nelkin, E., & Program, N. C. D. R. (2017). *Global Precipitation Climatology Project (GPCP) Climate Data Record (CDR), Version 1.3 (Daily)*. <https://doi.org/10.7289/V5RX998Z>
- AghaKouchak, A., Farahmand, A., Melton, F. S., Teixeira, J., Anderson, M. C., Wardlow, B. D., & Hain, C. R. (2015). Remote sensing of drought: Progress, challenges and opportunities. *Reviews of Geophysics*, 53, 452–480. <https://doi.org/10.1002/2014RG000456>
- Anderson, R., Lo, M.-H., Swenson, S., Famiglietti, J., Tang, Q., Skaggs, T., et al. (2015). Using satellite-based estimates of evapotranspiration and groundwater changes to determine anthropogenic water fluxes in land surface models. *Geoscientific Model Development*, 8(10), 3021–3031. <https://doi.org/10.5194/gmd-8-3021-2015>

- Ashouri, H., Hsu, K.-L., Sorooshian, S., Braithwaite, D. K., Knapp, K. R., Cecil, L. D., et al. (2015). PERSIANN-CDR: Daily precipitation climate data Record from multisatellite observations for hydrological and climate studies. *Bulletin of the American Meteorological Society*, 96(1), 69–83. <https://doi.org/10.1175/BAMS-D-13-00068.1>
- Bonfils, C., & Lobell, D. (2007). Empirical evidence for a recent slowdown in irrigation-induced cooling. *Proceedings of the National Academy of Sciences of the United States of America*, 104(34), 13582–13587. <https://doi.org/10.1073/pnas.0700144104>
- Brocca, L., Filippucci, P., Hahn, S., Ciabatta, L., Massari, C., Camici, S., et al. (2019). SM2RAIN—ASCAT (2007–2018): Global daily satellite rainfall data from ASCAT soil moisture observations. *Earth System Science Data*, 11(4), 1583–1601. <https://doi.org/10.5194/essd-11-1583-2019>
- Brocca, L., Moramarco, T., Melone, F., & Wagner, W. (2013). A new method for rainfall estimation through soil moisture observations. *Geophysical Research Letters*, 40, 853–858. <https://doi.org/10.1002/grl.50173>
- Brocca, L., Pellarin, T., Crow, W. T., Ciabatta, L., Massari, C., Ryu, D., et al. (2016). Rainfall estimation by inverting SMOS soil moisture estimates: A comparison of different methods over Australia. *Journal of Geophysical Research: Atmospheres*, 121, 12062–12079. <https://doi.org/10.1002/2016JD025382>
- Brocca, L., Tarpanelli, A., Filippucci, P., Dorigo, W., Zaussinger, F., Gruber, A., & Fernández-Prieto, D. (2018). How much water is used for irrigation? A new approach exploiting coarse resolution satellite soil moisture products. *International Journal of Applied Earth Observation and Geoinformation*, 73, 752–766. <https://doi.org/10.1016/j.jag.2018.08.023>
- Cao, B., Gruber, S., Zheng, D., & Li, X. (2020). The ERA5-Land soil temperature bias in permafrost regions. *The Cryosphere*, 14(8), 2581–2595. <https://doi.org/10.5194/tc-14-2581-2020>
- Chan, S., Bindlish, R., O'Neill, P., Jackson, T., Njoku, E., Dunbar, S., et al. (2018). Development and assessment of the SMAP enhanced passive soil moisture product. *Remote Sensing of Environment*, 204, 931–941. <https://doi.org/10.1016/j.rse.2017.08.025>
- Chen, Y., Feng, X., Fu, B., Shi, W., Yin, L., & Lv, Y. (2019). Recent global cropland water consumption constrained by observations. *Water Resources Research*, 55, 3708–3738. <https://doi.org/10.1029/2018WR023573>
- Ciabatta, L., Marra, A. C., Panegrossi, G., Casella, D., Sanò, P., Dietrich, S., et al. (2017). Daily precipitation estimation through different microwave sensors: Verification study over Italy. *Journal of Hydrology*, 545, 436–450. <https://doi.org/10.1016/j.jhydrol.2016.12.057>
- Clark, J. S., & Gelfand, A. E. (2006). A future for models and data in environmental science. *Trends in Ecology & Evolution*, 21(7), 375–380. <https://doi.org/10.1016/j.tree.2006.03.016>
- Dari, J., Brocca, L., Quintana-Seguí, P., Escorihuela, M. J., Stefan, V., & Morbidelli, R. (2020). Exploiting high-resolution remote sensing soil moisture to estimate irrigation water amounts over a mediterranean region. *Remote Sensing*, 12(16), 2593. <https://doi.org/10.3390/rs12162593>
- Dorigo, W., Scipal, K., Parinussa, R. M., Liu, Y. Y., Wagner, W., de Jeu, R. A. M., & Naeimi, V. (2010). Error characterisation of global active and passive microwave soil moisture datasets. *Hydrology and Earth System Sciences*, 14(12), 2605–2616. <https://doi.org/10.5194/hess-14-2605-2010>
- Dorigo, W., Wagner, W., Albergel, C., Albrecht, F., Balsamo, G., Brocca, L., et al. (2017). ESA CCI soil moisture for improved Earth system understanding: State-of-the art and future directions. *Remote Sensing of Environment*, 203, 185–215. <https://doi.org/10.1016/j.rse.2017.07.001>
- Famiglietti, J. S., Lo, M., Ho, S. L., Bethune, J., Anderson, K., Syed, T. H., & Rodell, M. (2011). Satellites measure recent rates of groundwater depletion in California's central valley. *Geophysical Research Letters*, 38, L03403. <https://doi.org/10.1029/2010GL046442>
- Fernandez-Moran, R., Al-Yaari, A., Mialon, A., Mahmoodi, A., Al Bitar, A., De Lannoy, G., et al. (2017). SMOS-IC: An alternative SMOS soil moisture and vegetation optical depth product. *Remote Sensing*, 9(5), 457. <https://doi.org/10.3390/rs9050457>
- Filippucci, P., Tarpanelli, A., Massari, C., Serafini, A., Strati, V., Alberi, M., & Brocca, L. (2020). Soil moisture as a potential variable for tracking and quantifying irrigation: A case study with proximal gamma-ray spectroscopy data. *Advances in Water Resources*, 136, 103502. <https://doi.org/10.1016/j.advwatres.2019.103502>
- Fisher, J. B., Lee, B., Purdy, A. J., Halverson, G. H., Dohlen, M. B., Cawse-Nicholson, K., et al. (2020). Ecostress: Nasa's next generation mission to measure evapotranspiration from the international space station. *Water Resources Research*, 56, e2019WR026058. <https://doi.org/10.1029/2019WR026058>
- Fisher, J. B., Melton, F., Middleton, E., Hain, C., Anderson, M., Allen, R., et al. (2017). The future of evapotranspiration: Global requirements for ecosystem functioning, carbon and climate feedbacks, agricultural management, and water resources. *Water Resources Research*, 53, 2618–2626. <https://doi.org/10.1002/2016WR020175>
- Fisher, J. B., Tu, K. P., & Baldocchi, D. D. (2008). Global estimates of the land-atmosphere water flux based on monthly AVHRR and ISLSCP-II data, validated at 16 FLUXNET sites. *Remote Sensing of Environment*, 112(3), 901–919. <https://doi.org/10.1016/j.rse.2007.06.025>
- Foley, J. A., Ramankutty, N., Brauman, K. A., Cassidy, E. S., Gerber, J. S., Johnston, M., et al. (2011). Solutions for a cultivated planet. *Nature*, 478(7369), 337–342. <https://doi.org/10.1038/nature10452>
- Font, J., Boutin, J., Reul, N., Spurgeon, P., Ballabriga-Poy, J., Chuprin, A., et al. (2013). SMOS first data analysis for sea surface salinity determination. *International Journal of Remote Sensing*, 34(9–10), 3654–3670. <https://doi.org/10.1080/01431161.2012.716541>
- Gelaro, R., McCarty, W., Suárez, M. J., Todling, R., Molod, A., Takacs, L., et al. (2017). The Modern-Era Retrospective analysis for research and applications, version 2 (MERRA-2). *Journal of Climate*, 30(14), 5419–5454. <https://doi.org/10.1175/JCLI-D-16-0758.1>
- Grafton, R. Q., Williams, J., Perry, C. J., Molle, F., Ringler, C., Steduto, P., et al. (2018). The paradox of irrigation efficiency. *Science*, 361(6404), 748–750. <https://doi.org/10.1126/science.aat9314>
- Huffman, G. J., Bolvin, D. T., Nelkin, E. J., Wolff, D. B., Adler, R. F., Gu, G., et al. (2007). The TRMM Multisatellite Precipitation Analysis (TMPA): Quasi-global, multiyear, combined-sensor precipitation estimates at fine scales. *Journal of Hydrometeorology*, 8(1), 38–55. <https://doi.org/10.1175/JHM560.1>
- Jägermeyr, J., Gerten, D., Heinke, J., Schaphoff, S., Kummu, M., & Lucht, W. (2015). Water savings potentials of irrigation systems: Global simulation of processes and linkages. *Hydrology and Earth System Sciences*, 19(7), 3073–3091. <https://doi.org/10.5194/hess-19-3073-2015>
- Jägermeyr, J., Pastor, A., Biemans, H., & Gerten, D. (2017). Reconciling irrigated food production with environmental flows for sustainable development goals implementation. *Nature Communications*, 8(1), 15900. <https://doi.org/10.1038/ncomms15900>
- Jalilvand, E., Tajrishy, M., Ghazi Zadeh Hashemi, S. A., & Brocca, L. (2019). Quantification of irrigation water using remote sensing of soil moisture in a semi-arid region. *Remote Sensing of Environment*, 231, 111226. <https://doi.org/10.1016/j.rse.2019.111226>
- Joyce, R. J., Janowiak, J. E., Arkin, P. A., & Xie, P. (2004). CMorph: A method that produces global precipitation estimates from passive microwave and infrared data at high spatial and temporal resolution. *Journal of Hydrometeorology*, 5(3), 487–503. [https://doi.org/10.1175/1525-7541\(2004\)005<0487:cmorph>2.0.co;2](https://doi.org/10.1175/1525-7541(2004)005<0487:cmorph>2.0.co;2)
- June, T., Evans, J. R., & Farquhar, G. D. (2004). A simple new equation for the reversible temperature dependence of photosynthetic electron transport: A study on soybean leaf. *Functional Plant Biology*, 31(3), 275. <https://doi.org/10.1071/FP03250>
- Keating, E. H., Doherty, J., Vrugt, J. A., & Kang, Q. (2010). Optimization and uncertainty assessment of strongly nonlinear groundwater models with high parameter dimensionality. *Water Resources Research*, 46, 2009WR008584. <https://doi.org/10.1029/2009WR008584>

- Kim, S., Parinussa, R. M., Liu, Y. Y., Johnson, F. M., & Sharma, A. (2015). A framework for combining multiple soil moisture retrievals based on maximizing temporal correlation. *Geophysical Research Letters*, 42, 6662–6670. <https://doi.org/10.1002/2015GL064981>
- Kueppers, L. M., Snyder, M. A., & Sloan, L. C. (2007). Irrigation cooling effect: Regional climate forcing by land-use change. *Geophysical Research Letters*, 34, L03703. <https://doi.org/10.1029/2006GL028679>
- Kumar, S. V., Peters-Lidard, C. D., Santanello, J. A., Reichle, R. H., Draper, C. S., Koster, R. D., et al. (2015). Evaluating the utility of satellite soil moisture retrievals over irrigated areas and the ability of land data assimilation methods to correct for unmodeled processes. *Hydrology and Earth System Sciences*, 19(11), 4463–4478. <https://doi.org/10.5194/hess-19-4463-2015>
- Lawrence, D. M., Fisher, R. A., Koven, C. D., Oleson, K. W., Swenson, S. C., Bonan, G., et al. (2019). The community land model version 5: Description of new features, benchmarking, and impact of forcing uncertainty. *Journal of Advances in Modeling Earth Systems*, 11, 4245–4287. <https://doi.org/10.1029/2018MS001583>
- Lawston, P. M., Santanello, J. A., & Kumar, S. V. (2017). Irrigation signals detected from SMAP soil moisture retrievals. *Geophysical Research Letters*, 44, 11860–11867. <https://doi.org/10.1002/2017GL075733>
- Li, X., Cheng, G., Lin, H., Cai, X., Fang, M., Ge, Y., et al. (2018). Watershed system model: The essentials to model complex human-nature system at the river basin scale. *Journal of Geophysical Research: Atmospheres*, 123, 3019–3034. <https://doi.org/10.1002/2017JD028154>
- Li, X., Jiang, W., & Duan, D. (2020). Spatio-temporal analysis of irrigation water use coefficients in China. *Journal of Environmental Management*, 262, 110242. <https://doi.org/10.1016/j.jenvman.2020.110242>
- Liu, Y., Dorigo, W., Parinussa, R., de Jeu, R., Wagner, W., McCabe, M., et al. (2012). Trend-preserving blending of passive and active microwave soil moisture retrievals. *Remote Sensing of Environment*, 123, 280–297. <https://doi.org/10.1016/j.rse.2012.03.014>
- Ma, N., Szilagyi, J., & Zhang, Y. (2021). Calibration-free complementary relationship estimates terrestrial evapotranspiration globally. *Water Resources Research*, 57, e2021WR029691. <https://doi.org/10.1029/2021WR029691>
- Michel, D., Jiménez, C., Miralles, D. G., Jung, M., Hirschi, M., Ershadi, A., et al. (2016). The WACMOS-ET project—Part 1: Tower-scale evaluation of four remote-sensing-based evapotranspiration algorithms. *Hydrology and Earth System Sciences*, 20(2), 803–822. <https://doi.org/10.5194/hess-20-803-2016>
- Mu, Q., Zhao, M., & Running, S. W. (2011). Improvements to a MODIS global terrestrial evapotranspiration algorithm. *Remote Sensing of Environment*, 115(8), 1781–1800. <https://doi.org/10.1016/j.rse.2011.02.019>
- Ozdogan, M., & Gutman, G. (2008). A new methodology to map irrigated areas using multi-temporal MODIS and ancillary data: An application example in the continental US. *Remote Sensing of Environment*, 112(9), 3520–3537. <https://doi.org/10.1016/j.rse.2008.04.010>
- Parinussa, R. M., Holmes, T. R. H., Wanders, N., Dorigo, W. A., & de Jeu, R. A. M. (2015). A preliminary study toward consistent soil moisture from AMSR2. *Journal of Hydrometeorology*, 16(2), 932–947. <https://doi.org/10.1175/JHM-D-13-0200.1>
- Prakash, S. (2019). Performance assessment of CHIRPS, MSWEP, SM2RAIN-CCI, and TMPA precipitation products across India. *Journal of Hydrology*, 571, 50–59. <https://doi.org/10.1016/j.jhydrol.2019.01.036>
- Priestley, C. H. B., & Taylor, R. J. (1972). On the assessment of surface heat flux and evaporation using large-scale parameters. *Monthly Weather Review*, 100(2), 81–92. [https://doi.org/10.1175/1520-0493\(1972\)100<0081:taosh>2.3.co;2](https://doi.org/10.1175/1520-0493(1972)100<0081:taosh>2.3.co;2)
- Reichle, R. H., Liu, Q., Koster, R. D., Crow, W. T., De Lannoy, G. J. M., Kimball, J. S., et al. (2019). Version 4 of the SMAP level-4 soil moisture algorithm and data product. *Journal of Advances in Modeling Earth Systems*, 11, 3106–3130. <https://doi.org/10.1029/2019MS001729>
- Rogers, D. H. (1997). *Efficiencies and water losses of irrigation systems*. Cooperative Extension Service, Kansas State University.
- Schlesinger, W. H., & Jasechko, S. (2014). Transpiration in the global water cycle. *Agricultural and Forest Meteorology*, 189–190, 115–117. <https://doi.org/10.1016/j.agrformet.2014.01.011>
- Siebert, S., Burke, J., Faures, J.-M., Frenken, K., Hoogeveen, J., Döll, P., & Portmann, F. T. (2010). Groundwater use for irrigation—A global inventory. *Hydrology and Earth System Sciences*, 14(10), 1863–1880. <https://doi.org/10.5194/hess-14-1863-2010>
- Siebert, S., & Döll, P. (2010). Quantifying blue and green virtual water contents in global crop production as well as potential production losses without irrigation. *Journal of Hydrology*, 384(3–4), 198–217. <https://doi.org/10.1016/j.jhydrol.2009.07.031>
- Siebert, S., Henrich, V., Frenken, K., & Burke, J. (2013). *Update of the digital global map of irrigation areas to version 5*.
- Siebert, S., Kummu, M., Porkka, M., Döll, P., Ramankutty, N., & Scanlon, B. R. (2015). A global data set of the extent of irrigated land from 1900 to 2005. *Hydrology and Earth System Sciences*, 19(3), 1521–1545. <https://doi.org/10.5194/hess-19-1521-2015>
- Storn, R., & Price, K. (1997). Differential evolution—a simple and efficient heuristic for global optimization over continuous spaces. *Journal of Global Optimization*, 11(4), 341–359. <https://doi.org/10.1023/A:1008202821328>
- ter Braak, C. J. F., & Vrugt, J. A. (2008). Differential Evolution Markov chain with snooker updater and fewer chains. *Statistics and Computing*, 18(4), 435–446. <https://doi.org/10.1007/s11222-008-9104-9>
- Wada, Y., Bierkens, M. F. P., de Roo, A., Dirmeyer, P. A., Famiglietti, J. S., Hanasaki, N., et al. (2017). Human-water interface in hydrological modelling: Current status and future directions. *Hydrology and Earth System Sciences*, 21(8), 4169–4193. <https://doi.org/10.5194/hess-21-4169-2017>
- Wada, Y., van Beek, L. P. H., Wanders, N., & Bierkens, M. F. P. (2013). Human water consumption intensifies hydrological drought worldwide. *Environmental Research Letters*, 8(3), 034036. <https://doi.org/10.1088/1748-9326/8/3/034036>
- Wada, Y., Wisser, D., & Bierkens, M. F. P. (2014). Global modeling of withdrawal, allocation and consumptive use of surface water and groundwater resources. *Earth System Dynamics*, 5(1), 15–40. <https://doi.org/10.5194/esd-5-15-2014>
- Wagner, W., Hahn, S., Kidd, R., Melzer, T., Bartalis, Z., Hasenauer, S., et al. (2013). The ASCAT soil moisture product: A review of its specifications, validation results, and emerging applications. *Meteorologische Zeitschrift*, 22(1), 5–33. <https://doi.org/10.1127/0941-2948/2013/0399>
- Wang, G., Garcia, D., Liu, Y., de Jeu, R., & Johannes Dolman, A. (2012). A three-dimensional gap filling method for large geophysical datasets: Application to global satellite soil moisture observations. *Environmental Modelling & Software*, 30, 139–142. <https://doi.org/10.1016/j.envsoft.2011.10.015>
- Wei, Z., Yoshimura, K., Wang, L., Miralles, D. G., Jasechko, S., & Lee, X. (2017). Revisiting the contribution of transpiration to global terrestrial evapotranspiration. *Geophysical Research Letters*, 44, 2792–2801. <https://doi.org/10.1002/2016GL072235>
- Zaussinger, F., Dorigo, W., Gruber, A., Tarpanelli, A., Filippucci, P., & Brocca, L. (2019). Estimating irrigation water use over the contiguous United States by combining satellite and reanalysis soil moisture data. *Hydrology and Earth System Sciences*, 23(2), 897–923. <https://doi.org/10.5194/hess-23-897-2019>
- Zhang, C., & Long, D. (2021). Estimating spatially explicit irrigation water use based on remotely sensed evapotranspiration and modeled root zone soil moisture. *Water Resources Research*, 57, e2021WR031382. <https://doi.org/10.1029/2021WR031382>
- Zhang, K., Ma, J., Zhu, G., Ma, T., Han, T., & Feng, L. L. (2017). Parameter sensitivity analysis and optimization for a satellite-based evapotranspiration model across multiple sites using Moderate Resolution Imaging Spectroradiometer and flux data. *Journal of Geophysical Research: Atmospheres*, 122, 230–245. <https://doi.org/10.1002/2016JD025768>

- Zhang, K., Zhu, G., Ma, J., Yang, Y., Shang, S., & Gu, C. (2019). Parameter analysis and estimates for the MODIS evapotranspiration algorithm and multiscale verification. *Water Resources Research*, 55, 2211–2231. <https://doi.org/10.1029/2018WR023485>
- Zhang, L., Li, X., Cao, Y., Nan, Z., Wang, W., Ge, Y., et al. (2020). Evaluation and integration of the top-down and bottom-up satellite precipitation products over mainland China. *Journal of Hydrology*, 581, 124456. <https://doi.org/10.1016/j.jhydrol.2019.124456>
- Zheng, D., Li, X., Wang, X., Wang, Z., Wen, J., van der Velde, R., et al. (2019). Sampling depth of L-band radiometer measurements of soil moisture and freeze-thaw dynamics on the Tibetan Plateau. *Remote Sensing of Environment*, 226, 16–25. <https://doi.org/10.1016/j.rse.2019.03.029>
- Zhu, G., Li, X., Ma, J., Wang, Y., Liu, S., Huang, C., et al. (2018). A new moving strategy for the sequential Monte Carlo approach in optimizing the hydrological model parameters. *Advances in Water Resources*, 114, 164–179. <https://doi.org/10.1016/j.advwatres.2018.02.007>
- Zhu, G., Li, X., Su, Y. H., Zhang, K., Bai, Y., Ma, J. Z., et al. (2014). Simultaneously assimilating multivariate data sets into the two-source evapotranspiration model by Bayesian approach: Application to spring maize in an arid region of northwestern China. *Geoscientific Model Development*, 7(4), 1467–1482. <https://doi.org/10.5194/gmd-7-1467-2014>
- Zohaib, M., & Choi, M. (2020). Satellite-based global-scale irrigation water use and its contemporary trends. *Science of the Total Environment*, 714, 136719. <https://doi.org/10.1016/j.scitotenv.2020.136719>